Investigation of growth, structural and electronic properties of V_2O_3 thin films on selected substrates

Dissertation zur Erlangung des Doktorgrades der
Mathematisch-Naturwissenschaftlichen Fakultät der
Universität Augsburg

Vorgelegt von

Alexei Nateprov

August 2006

Erstgutachter: Prof. Dr. S. Horn
Zweitgutachter Priv.-Doz. Dr. Helmut Karl

Tag der Einreichung: 1 December 2006

Contents

Introduction

Transition metal oxides are of continuous interest in modern solid state physics due to their exceptional electronic, magnetic and optical properties [Goodenough1971]. Many transition metal oxides show phase transitions from metallic to insulating or semiconducting states. The electronic structure of these materials is strongly influenced by the partially filled *d*-orbitals and related strong Coulomb interaction [Mott1968].

Vanadium oxides are one the most typical examples of transition metal oxides. In particular, vanadium sesquioxide (V_2O_3) is often referred to as a prototype of a strongly correlated electron system. As firstly reported by M. Foex in 1946 [Foex1946], this compound shows a sharp metal to insulator (MI) transition at T_{MI}~160-170 K, quantified by a six orders of magnitude increase of the resistance. Since that time a lot of experimental and theoretical studies were done to understand the origin of this transition. However, a consistent model, accounting for the features of the MIT as well as of the related magnetic and structural phase transitions, is absent till now, thus making these phenomena and the material itself still highly actual nowadays.

The present work is devoted to the experimental study of the MI transition in V_2O_3 thin films, grown on different substrates. Why actually thin films? Firstly, this is because the thin film technology is mostly appropriated for any device applications. Secondly, the study of the MIT transition in bulk V_2O_3 is an extremely delicate issue, because of an practically unavoidable crash of the sample during the cooling and heating cycles due to large volume change across the metal to insulator transition. Thin film technologies make it possible to accommodate the above stress, thus providing stable samples for experimental studies as well as planar device structures for applications. Very interesting for applications seems to be V_2O_3 films grown on diamond substrates. Due to high value of the energy gap in diamond, optical filtering, based on the change of

optical constants in V_2O_3 thin films across the MI transition looks promising. Other applications include infra-red mirrors, resistive transducers, etc.

The main goal of this work was to develop a technology of growth of V_2O_3 thin films on substrates with different electrical and structural properties (diamond and $LiNbO_3$), designed for specific applications. Because of the large lattice mismatch between V_2O_3 and diamond, the film growth presents a rather complicated problem, which was not solved before the present work started.

Another important problem of growth technologies is the temperature of substrate during the deposition. Especially, because of high mobility of atoms of light elements (like Li) at higher temperatures, the diffusion of these elements into the growing film is enhanced, yielding a deterioration of the properties of V_2O_3. Thus, the conventional UHV techniques, which usually involve an in situ growth at high substrate temperatures, T_{Sub}=600 °C, cannot be applied in the case of diamond and $LiNbO_3$ substrates.

We present here a new growth strategy for V_2O_3 thin films, based also on the UHV technique, which successfully solves the above mentioned difficulties. Using this technology, thin films of V_2O_3 with reproducible parameters were grown on diamond and $LiNbO_3$ substrates for the first time. We have characterized in detail the structural and electrical properties of the obtained films with a special focus on their potential applications.

The present work is organized as follows. The "Basics" (Chapter 2) gives an introduction to the main properties of the V_2O_3 system, including the phase diagram, the crystal and electronic structure. In this part also the modes of thin film growth as well as the theory of surface acoustic waves are described.

The "Experimental" part (Chapter 3) includes the description of the film preparation and characterization techniques.

The structural properties, studied by dynamic secondary ion mass spectrometry (SIMS), X-ray powder diffraction (XRD), Rutherford backscattering spectrometry (RBS), atomic force microscopy (AFM), as well as electronic properties of the films are described in Chapter 4. In this chapter the results of the surface acoustic waves study are also presented.

2. Basics

2.1 Theoretical Approaches

The electronic properties of solid state systems can be described by the following *ab initio* Hamiltonian [Fazekas1999]

$$\hat{H} = \sum_{\sigma} \int d^3\mathbf{r}\hat{\Psi}^+(\mathbf{r},\sigma)\left[-\frac{\hbar^2}{2m_e}\Delta + V_{ion}(\mathbf{r})\right]\hat{\Psi}(\mathbf{r},\sigma) + \frac{1}{2}\sum_{\sigma\sigma'} \int d^3\mathbf{r}d^3\mathbf{r}'\hat{\Psi}^+(\mathbf{r},\sigma)\hat{\Psi}^+(\mathbf{r}',\sigma')V_{ee}(\mathbf{r}-\mathbf{r}')\hat{\Psi}(\mathbf{r}',\sigma')\hat{\Psi}(\mathbf{r},\sigma). \quad (2.1.1)$$

Here, $\hat{\Psi}^+$ is field operator that creates an electron, $\hat{\Psi}$ is the field operator that annihilates an electron at position $\boldsymbol{r}$ with spin σ, Δ is the Laplace operator, m_e is the electron mass, e is the electron charge. V_{ion} denotes the one-particle ionic potential of all ions with charge eZ_i at given positions $\boldsymbol{R}_i$ via

$$V_{ion}(\mathbf{r}) = -e^2\sum_i \frac{Z_i}{|\mathbf{r}-\mathbf{R}_i|} \quad (2.1.2)^*$$

and

---

* For SI system the right part should be multiplyed by a factor of $\frac{1}{4\pi\varepsilon_0}$

$$V_{ee}(\mathbf{r}-\mathbf{r}') = \frac{e^2}{2}\sum_{\mathbf{r}\neq\mathbf{r}'} \frac{1}{|\mathbf{r}-\mathbf{r}'|} \tag{2.1.3}$$

is the electron-electron interaction potential.

Although the Hamiltonian has a quite simple form it is not possible to solve it exactly (without any approximations) if there are more than a few electrons involved. In particular, up to now such numerical calculations have been done only for the simplest few-electrons chemical compounds (like atomic or molecular hydrogen and helium).

During the last century, several methods have been developed to solve this Hamiltonian approximately [Koln1999]. In particular, as a first approximation the nuclei and electrons can be treated independently. This so-called Born-Oppenheimer [Born1927] approximation significantly simplifies the calculations, however, the obtained Hamiltonian cannot be solved exactly and further approximations are required.

One of the most common of them is the so-called one-electron approximation, where the many-electron system is described by non-interacting electrons moving in an effective average potential of all electrons. The one-electron wave function can be found by solving the one-electron Schrödinger equation with an effective mean-field potential, which depends on the interaction between the electrons as well. Although the potential and wave functions are unknown at the beginning, these equations should be solved self-consistently.

One of the first known approximations for an effective potential was the so-called Hartree-Fock approximation [Hartree1958], [Fock1930] which describes both Coulomb and exchange electron correlation. This method is appropriate to describe the correlated electron systems with a long-range order (magnetic Mott insulators and charge ordered systems). However, in the Hartree-Fock method the Coulomb interaction is unscreened and this unscreened value of Coulomb parameter is rather large (15 - 20 eV), while screening for 3d transition metals leads to much smaller values of 4 - 6 eV, observed in experiments. Because of neglecting of screening effects, the Hartree-Fock approximation usually overestimates the energy gap by a factor of 2 - 3 with respect to experimental data.

An alternative approach to treat the effective potential is provided by the density functional theory (DFT) where the electron density-distribution rather

then the many body wave function plays a crucial role. In DFT the total energy function is written as a functional of electron density, although the limitations of this theory come from the lack of knowledge of an exact form of the exchange-correlation functional. Therefore, in order to solve the DFT equations further approximation for the exchange-correlation potential should be made. The simplest and one of the most robust of them is the so-called local density approximation (LDA) in which the many-electron problem is mapped onto a non-interacting system with one electron exchange-correlation potential same as in the homogeneous electron gas [von Barth1972] [Jones1989]. In the last several decades this method has been proved to be highly successful for realistic calculations of many weakly correlated systems, like extended molecules, metal and band insulators. On the other hand, in strongly correlated systems with partially filled *d, f* electron shells where the Coulomb repulsion is comparable with the bandwidth (transition metal oxides, rare-earth metal compounds, and heavy fermion systems, etc) the application of this theory is problematic.

Although, there were several attempts to improve the LDA (e.g. the self-interaction method, LDA with Hubbard Coulomb interaction correction (LDA+U), etc.) all of them are not able to describe the many-electron phenomena like Kondo-effect or the quasiparticle peak in the spectral function of strongly correlated metals. In this respect, the model Hamiltonian approach is much more powerful than the methods mentioned above.

In the model approach instead of making approximations and trying to solve the Hamiltonian directly as done in DFT, the complicated electron-electron interaction term, which describes the interplay of each electron with every other electron, is replaced by a purely local term [Hubbard1963], [Kanamori1963] and [Gutzwiller1963]. In addition to this interaction between the electrons on the same lattice site isotropic hopping to nearest neighbors is allowed. The Hamiltonian of the one-band Hubbard model can be written as

$$\hat{H} = -t \sum_{\langle ij \rangle, \sigma} \hat{c}^{+}_{i\sigma} \hat{c}_{j\sigma} + U \sum_{i} \hat{n}_{i\uparrow} \hat{n}_{i\downarrow}. \qquad (2.1.4)$$

where $\hat{c}^{+}_{i\sigma}$ ($\hat{c}_{j\sigma}$) creates (destroys) an electron at site *i* (*j*) with spin σ, a lattice site is labeled by index j, and $\hat{n}_{j\sigma} = c^{+}_{j\sigma} c_{j\sigma}$ is the corresponding occupation number

operator. The first sum is restricted to the nearest-neighbor pairs $\langle i, j \rangle$ and describes the kinetic energy (hopping) of electrons. The interaction term (second sum) describes the Coulomb repulsion between electrons sharing the same orbital (the Pauli principle requires them to have opposite spins), with the Hubbard U defined as:

$$U = \int d\mathbf{r}_1 \int d\mathbf{r}_2 \left|\phi(\mathbf{r}_1 - \mathbf{R}_j)\right|^2 \frac{e^2}{\left|\mathbf{r}_1 - \mathbf{r}_2\right|} \left|\phi(\mathbf{r}_2 - \mathbf{R}_j)\right|^2 . \qquad (2.1.5)$$

However, the systems of our particular interest, *3d* transition metal oxides, have five *d* - bands, originated from a cubic crystal field splited triplet t_{2g} - and duplet e_g^σ - states. Therefore, a one-band Hubbard model is not sufficient to describe these materials in which, at least, the Hunds rule coupling (J) that energetically favours aligned spins is of strong importance. Including those interactions a multi-band Hubbard model can be written as:

$$\hat{H} = \sum_{\mathbf{k},m\sigma} \varepsilon_{\mathbf{k}m} \hat{c}^+_{\mathbf{k}m\sigma} \hat{c}_{\mathbf{k}m\sigma} + U \sum_{im} \hat{n}_{im\downarrow} \hat{n}_{im\uparrow} + \frac{1}{2} {\sum_{i,mm',\sigma\sigma'}}' (U' - \delta_{\sigma\sigma'} J) \hat{n}_{im\sigma} \hat{n}_{im'\sigma'} . \qquad (2.1.6)$$

The solution of the Hubbard model is highly non-trivial because of the fact that the interaction and hopping terms do not commute, and additional approximations are needed, where among the most successful is the dynamical mean field theory (DMFT) developed in the last decade. The basis of DMFT, a non perturbative approach for solving strongly correlated electron system, is mapping of the lattice (Hubbard) model onto the Anderson impurity model. This simplifies the spatial dependence of the correlations among electrons and accounts fully their dynamics. It becomes exact in the limit of infinite dimensions or infinite lattice coordination number.

Applications of DMFT have led to a lot of progress in solving many of the problems inherent to strongly correlated electron systems. Among them the Mott

metal-insulator transition, is one of the central problems of modern solid state physics that addresses directly the competition between kinetic and correlation energy – i.e. the wave and particle like character of electrons in the solid. Within DMFT, the Mott metal-insulator transition occurs when the electron interactions are sufficiently strong to case the quasiparticle peak to vanish as the spectral weight-frequency Hubbard bands.

This is schematically presented in Fig. 2.1.1, which shows the variation of the spectral function (density of states) with increasing the ratio of the correlation strength U to bandwidth W. Taking into account different temperatures this qualitative picture evolves in the phase diagram presented in Fig. 2.1.2.

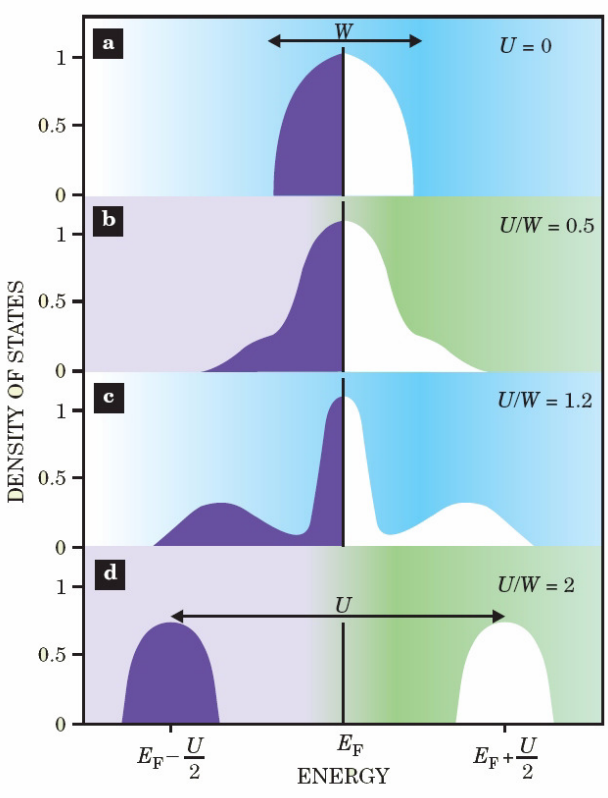

Fig. 2.1.1. *The density of states (DOS) of electrons in a material varies as a function of the local Coulomb interactions between them. This series illustrates how the spectral features evolve in the DMF solution of the Hubbard model at zero temperature and half filling (the same number of electrons as lattice sites) [Kotliar2004].*

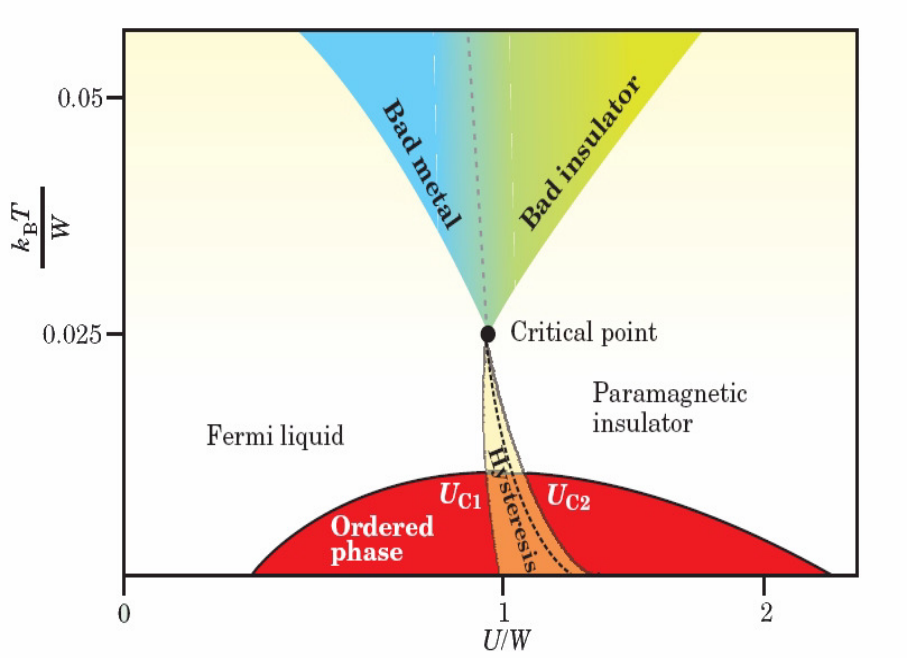

Fig. 2.1.2. *Schematic phase diagram of the material undergoing a Mott metal-insulator transition. Temperature and the strength of Coulomb repulsion U are plotted for a correlated electron material that is described using a Hubbard model. At low temperature, the system has long-range order (red) according to solutions of the DMFT; the type of ordering is material- and model-dependent. In the orange region, the model has two distinct paramagnetic solutions bounded by the lines U_{c1} (where the insulator disappears) and U_{c2} (where the metal disappears). In equilibrium, a dotted first order phase transition boundary indicates the position at which the free energy of these two solutions crosses. The first-order line terminates at a second order critical point. At higher temperatures, the phase diagram is more universal. Two crossover regimes indicate the change in materials properties as the electron interactions increase from left to right. The first illustrates the crossover from a Fermi liquid to a bad metal (blue), in which the resistivity in anomalously large. In the second crossover, materials take on the properties of a bad insulator (green), in which the resistivity decreases with increasing temperature [Kotliar2004].*

During last decades many efforts have been made to verify the surprising aspects of the theory of the Mott transition in strongly correlated electron systems. Definitely, V_2O_3 is the most typical and important example of such a system.

2.2 The V_2O_3 System

2.2.1 Phase Diagram

Since M. Foex [Foex1946] in 1946 has discovered experimentally in V_2O_3 a sharp temperature-induced metal-insulator transition (MIT) this compound attracts considerable scientific interest. Later on it was found that the temperature of the MIT can be influenced by means of hydrostatic pressure and uniaxial stress [Feinleib1967] as well as by doping with chromium [McWhan70] or titanium [McWhan71]. These dependencies were studied systematically by McWhan *et al*. resulting in the following phase diagram (Fig. 2.2.1.1).

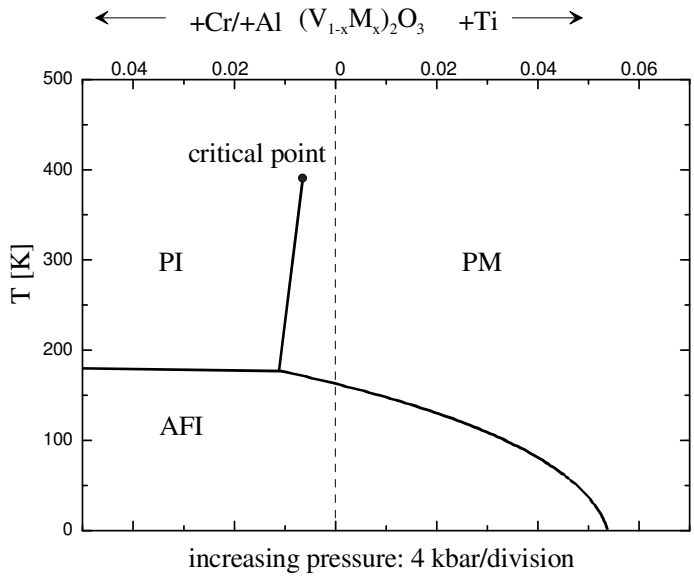

Fig. 2.2.1.1. *Phase diagram for MIT in V_2O_3 as a function of doping with Cr or Ti and as a function of pressure [McWhan 70].*

This diagram contains three regions:

- Paramagnetic metallic phase (PM)
- Antiferromagnetic insulating phase (AFI)
- Paramagnetic insulating phase (PI)

Stoichiometric V_2O_3 is a paramagnetic metal (PM) at room temperature. With decreasing temperature below the transition temperature (T_{MIT}) of approximately 160 K, V_2O_3 becomes an antiferromagnetic insulator (AFI). Moreover, the MIT is accompanied by the change of the crystal structure. By increasing the pressure or Ti doping, the MIT shifts down to lower temperatures and for pressures exceeding 22 kbar, or concentrations of Ti higher than 4%, the AFI phase is completely suppressed.

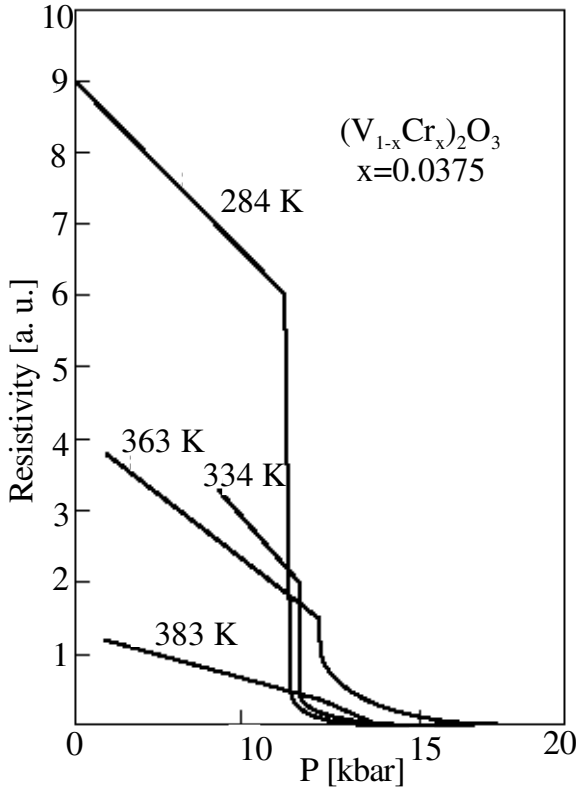

Fig. 2.2.1.2. *Pressure dependence of the resistivity of Cr-doped V_2O_3 [Jayaraman1970].*

The hydrostatic pressure induced drop of the resistance for Cr-doped V_2O_3 at MIT is about two orders of magnitude near room temperature (see Fig. 2.2.1.2) [Jayaraman1970]. With increasing temperature the resistivity jump decreases, and vanishes at about 393 K, which corresponds to the critical point in Fig. 2.2.1.2.

Another important parameter which can affect the MIT is stoichiometry. McWhan *et al*. have investigated the dependence of the transition temperature on the stoichiometry and measured the electrical resistivity of V_2O_{3+x} ($0 \leq x \leq 0.12$) [McWhan1971a]. They found that the temperature of the transition from a paramagnetic metal to an antiferromagnetic insulator decreases rapidly with increasing x (Fig. 2.2.1.3), and the insulating state is suppressed for $x \geq 0{,}04$.

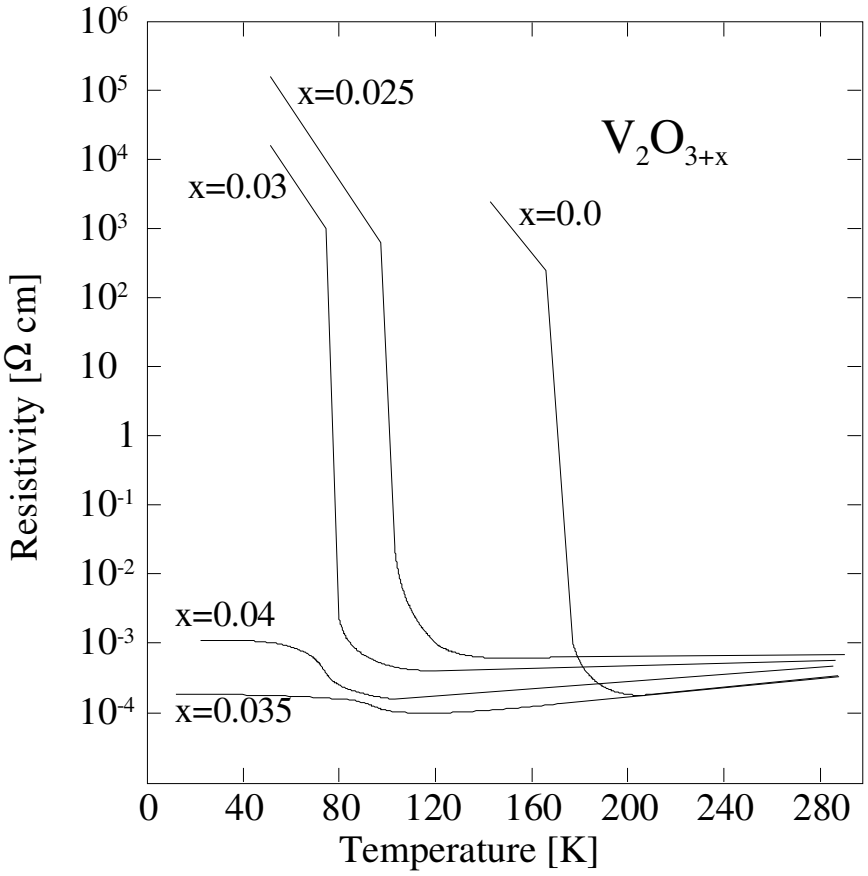

Fig. 2.2.1.3. *Dependence of the transition temperature on stoichiomentry for pressed powder samples of V_2O_{3+x}. [McWhan1971].*

2.2.2 Crystal Structure

At room temperature in the paramagnetic metallic phase V_2O_3 has a corundum structure with space group $R\bar{3}c$ (Fig. 2.2.2.1). The corundum structure is commonly described as a hexagonal structure with lattice constants a = 4.9515 Å and c = 14.003 Å [Dernier1970a].

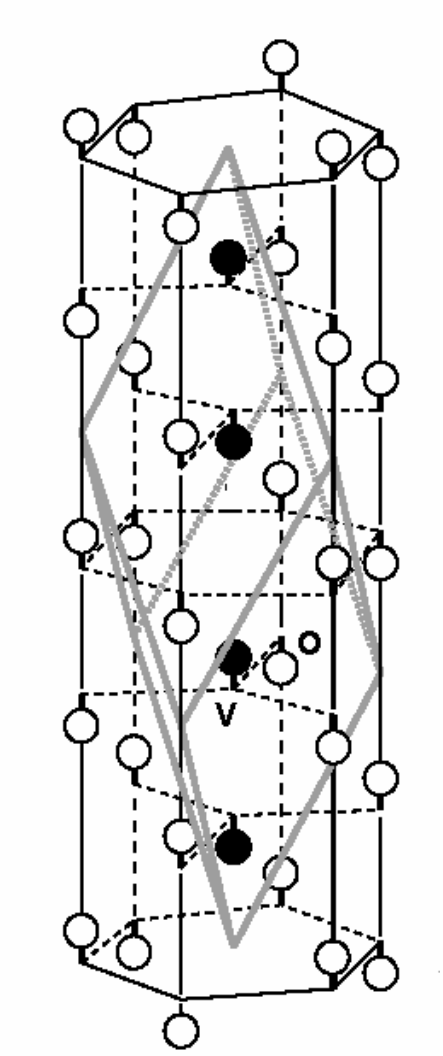

Fig. 2.2.2.1. *Hexagonal unit cell with inscribed trigonal primitive cell of V_2O_3 in the corundum phase [Kuroda1977].*

Along the hexagonal *c*-axis every third vanadium place is vacant (Fig. 2.2.2.2). In the plane perpendicular to the *c*-axis (so called *basal plane*) one can find 3 cations (Fig. 2.2.2.2 V_2 and V_{2a}), which have the same distance from V_0. All vanadium atoms are surrounded by an oxygen octahedron (shown in Fig. 2.2.2.2 for the V_0 atom only) and this oxygen octahedron is skewed about the central vanadium atom, while the average V - V distance remains essentially constant.

For temperatures below the metal to insulator transition (~ 160 K), the corundum structure of V_2O_3 distorts, lowering the symmetry down to monoclinic.

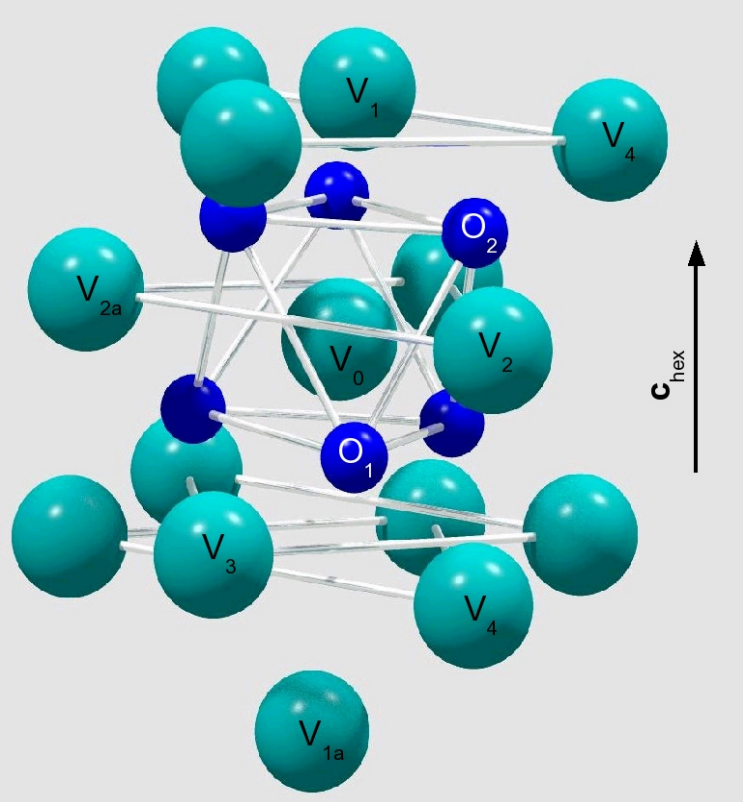

Fig. 2.2.2.2. *Crystal structure of V_2O_3 [Pfalzer2004].*

The distortion increases during the phase transition from the paramagnetic metallic phase (PM) into the paramagnetic insulating (PI) phase but without a change of the distance between the oxygen ions and the central V ion. Therefore the distortion is called to be „umbrella-like“: Oxygen ions behave like being

mounted onto the spokes of a umbrella which is opened or closed. Reason for the increase of the trigonal distortion of the coordination octahedron is an increase in V_0 - V_1 distance. This also elucidates according to Dernier [Dernier 1970b], why the c_{hex} axis in PI-phase is dramatically shortened while the a_{hex} axis practically keeps its length.

The transition from the PM to the AFI-phase accompanies with two substantial structural changes. Firstly, the c_{hex} axis tilts about 2° against the normal of the basal plane and, secondly, the V_0 - V_1 pairs rotate in the monocline *a* - *c* plane about 1.6° along the same direction Therefore the V_0 - V_1 distance is increasing like at the PM – PI phase transition. On the other hand, the three-fold symmetry in the *basal* plane is broken due to the b_{hex} vector getting extended, while a_{hex} stays constant. Because of this the V_0 - V_{2a} distance increases distinctly (about 0.1 Å), while the two other V_0 - V_2 distances almost stay the same.

The information on the crystal structure presented so far was obtained by X-ray diffraction measurements, which hold conclusions only on the long range order of a crystal and do not contain information about the local order like disorder or fluctuations. To investigate further on local structure Frenkel *et al.* [Frenkel 1997] performed Extended X-ray Absorption Fine Structure (EXAFS) measurements on V_2O_3. These measurements show that in the nearest neighbourhood of the vandium ions the trigonal symmetry is broken in the paramagnetic metallic phase. Due to the fact that this break of symmetry cannot be detected by X-ray structural analysis, the size of monoclinically distorted domains was estimated to be about 7 Å to 40 Å.

2.2.3 Electronic Structure

In the octahedral oxygen coordination of V_2O_3 the cubic crystal field splits the five degenerate atomic V - *3d* bands into three degenerate t_{2g} and two degenerate e_g^{σ} - bands [Cox1992]. The trigonal distortion of the oxygen octahedra leads to further splitting of the t_{2g} - bands into one a_{1g} - and two degenerate e_g^{π} - bands. For the qualitative description of the metal-insulator transition several models were proposed. Goodenough [Goodenough1971] made one of the first attempts to

model the band structure of V_2O_3. He proposed a simple model where the a_{1g} orbital lies higher than the doubly degenerate e_g^{π}, and the isotropic metallic properties were explained by a small overlap with the bonding a_{1g} - band.

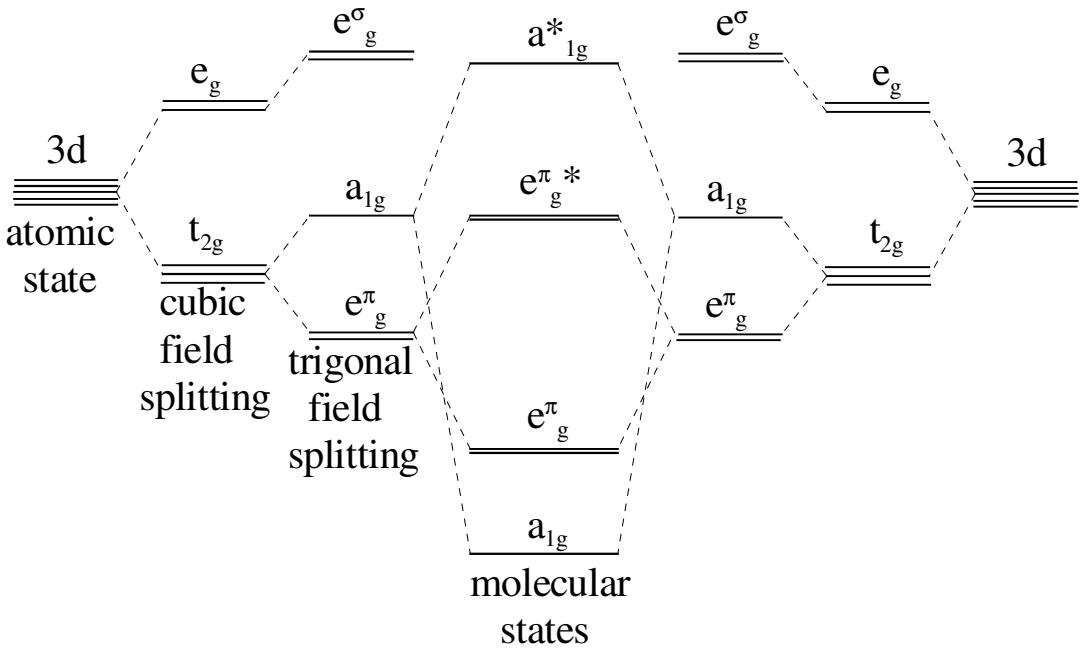

Fig. 2.2.3. *Model of the electronic structure of V_2O_3 according to Castellani et al. [Castellani1978a].*

In the model of Castellani et al. [Castellani1978a], [Castellani1978b] the a_{1g} orbital lies much lower than the e_g^{π} orbital which is fully occupied with two electrons. The remaining two electrons (one at each V site) occupies one of the two fold degenerate e_g^{π} orbitals, leading to a ground state with S=1/2 for each V site. This model of Castellani was the standard model for V_2O_3 for a long time and has been used to explain many experimental results [Fabrizio1998], [Paolasini1999].

During last couple of years new theoretical and experimental results questioned this model. Park et al. [Park2000] obtained from polarization dependence of the X-ray absorption measurements that the system has a spin 1 state. Furthermore they found that in the ground state the $e_g^{\pi}e_g^{\pi}$ states are dominating with a small

admixture of $a_{1g}e_g^{\pi}$. The LDA+U calculations made by Ezhov *et al.* [Ezhov1999] gave the similar results.

However still many theoretical investigations are using the idea of strong hybridization in V - V pair along the trigonal axis including a_{1g} intra-pair hopping and the inter-pair hopping is treated as a perturbation [Mila2002]. In this model studies the values of the hopping parameters are determined by a least-square fit of the LDA bands to model Hamiltonian with nearest neighbour hopping. Elfimov *et al*. [Elfimov2003] showed a significant reduction of $a_{1g} - a_{1g}$ hopping in the V - V pair if one takes into account next nearest neighbour hopping. That's why the inter-pair hopping cannot be considered as a small contribution and therefore it cannot be treated as a small perturbation in the theoretical calculation.

2.3 Thin Films Growth Modes

Fig. 2.3.1 illustrates typical processes that may occur during thin film growth. Once atoms are on the surface they may diffuse, can meet other adatoms to form a dimer (a) or attach to existing islands (b). Once adatoms are attached to an island, they can detach from the island edge (c) or diffuse along the island edge (d). Deposition of adatoms on top of islands and corresponding processes have to be considered (e), (f). At high temperature some adatoms can re-evaporate (g) [Ratsch2003].

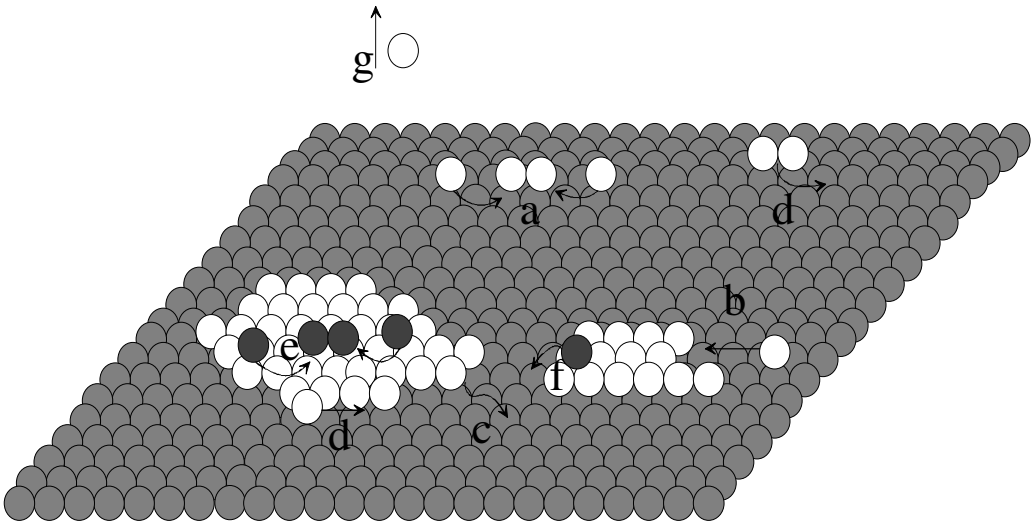

Fig. 2.3.1. *Schematic view of typical atomistic processes during thin film growth [Ratsch2003].*

Thin films grow on a substrate because of the adsorption of atoms from an supersaturated vapor phase, which in addition should be very pure. To achieve this, the evaporation and adsorption processes should be performed under high (HV) or ultrahigh (UHV) vacuum conditions. The atoms adsorbed at the substrate diffuse on the surface and arrange themselves depending on the temperature and

specific substrate-film interaction. This interaction can be characterized by three parameters: the surface free energy of the substrate (σ_{sub}), the surface energy of the deposited film material (σ_{film}) and the interface energy between the substrate and deposited film (σ_{ia}).

Experimentally three types of growth of thin films were observed:

- (a) Layer-by-layer deposition or Frank-van der Merwe growth.
- (b) Island or Vollmer-Weber growth.
- (c) Layer-plus-island growth or Stransky-Krastanov growth.

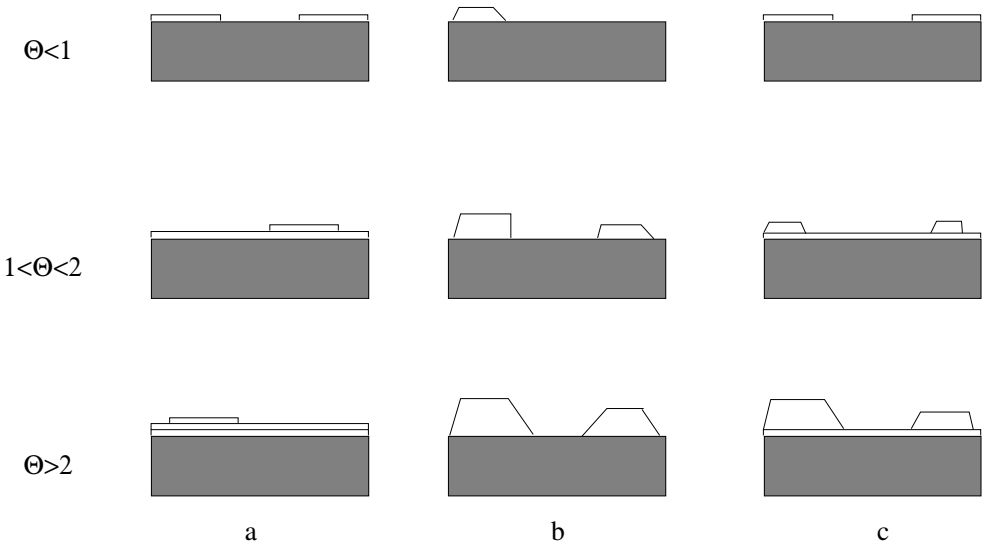

Fig. 2.3.2. *Schematic view of the three growth modes. a-Frank-van der Merwe, b-Volmer-Weber, c-Stransky-Krastanov (Θ is the covering, which represents the number of mono-layers of growing film.)*

The most important is the Frank-van der Merwe mode, or layer-by-layer growth [Frank 1949]. In this mode the interaction between substrate and adsorbed particles is much larger than the interaction between the nearest particles of growing film ($\sigma_{film}<\sigma_{sub}+\sigma_{ta}$). In this case it is energetically favorable for the deposited material to cover the substrate completely. This is equivalent to perfect "wetting" the substrate by the film material. In this mode atoms deposited on top of existing two-dimensional islands (one atom thick) have to be able to descend from these islands and fill the lowest level (Fig. 2.3.2a).

Under inverse condition, i.e. when interaction between adsorbed particles is stronger than the interaction between the particles and substrate ($\sigma_{film}>\sigma_{sub}+\sigma_{ia}$) the Vollmer-Weber growth or three-dimensional (3D) island nucleation takes place. In this case the deposited material form 3D islands on the substrate (Fig. 2.3.2b), in order to minimize the surface of the deposited material, and thereby to minimize the energy. One can say that the film dies not "wet" the substrate.

The most complex situation is when the surface energies of the deposited material and the substrate are more or less equal. If the lattice matching is not perfect, strain will be accumulated in the layer, which will cause an increase in energy for the total system. If the strain energy is too large, the system will try to rearrange itself to find a lower energy state. This can be done in several ways, for example by creating misfit dislocations. Another way is to form 3D islands. The strain energy increases linearly with the thickness of the layer according to

$$E = \mu\varepsilon^2 d \tag{2.3}$$

Here, μ is the elastic modulus, ε is the lattice mismatch, and d is the thickness.

When the strain has built up to a certain level, i.e. at a certain critical thickness of the grown layer, the system will become unstable and a rearrangement to lower energy configurations will be possible.

In the case of a small lattice mismatch, i.e. the critical thickness is large, the change in the growth configuration is often mediated by the creation of misfit dislocations. However, for large lattice mismatch (2 - 10%) and compressive strain in the growing layer, there is the possibility that the strain relaxation will take place via the formation of 3D islands. The islands will to a large extent be built up from material from the decomposing, critically strained, epi-layer. After the transition is complete, the result will be a thin 2D layer, called wetting layer, and on top of that, 3D islands (Fig. 2.3.2c). This growth mode is called Stranski-Krastanow. If the lattice mismatch is larger than 10% the island formation usually occurs directly on the substrate, without any wetting layer, i.e. the Volmer Weber growth mode.

2.4 Surface Acoustic Waves

As has been discussed in Chapter 2.1, V_2O_3 shows a metal to insulator transition (MIT) which occurs at $T_{MI} \approx 160$ K on cooling [Foex1946] [Morin1959]. The MIT involves an intimate interplay between structural, electronic and magnetic degrees of freedom [McWhan73], resulting in a complexity of physical phenomena. At the transition, the crystal lattice transforms from trigonal to monoclinic with an increase of the volume in the percentage range [Frenkel1997]. The MIT has been studied experimentally by a number of methods, however it is a long standing yet not completely resolved issue. One of the main problems to study the MIT systematically is related to the crash of the sample during the cooling and heating cycles. The advantage of thin films is that structural integrity of sample is not affected by passing the transition, perhaps due to the stabilization by the substrate. This allows the investigation of such films by surface acoustic waves (SAW)

The material displacements are illustrated further in Fig. 2.4.1, which shows the distortion at an instant of time of a rectangular grid in a sagittal plane section of the substrate as produced by a Rayleigh wave [Matthews1977]. The time and phase quadrature of the displacements are evident along with the retrograde elliptical displacement of a point on the surface. The displacement amplitudes are greatly exaggerated in the diagram. In practical devices such amplitudes are very small with respect to the wavelength of the order of 10^{-5} λ.

The displacement components of a Rayleigh wave propagating with phase velocity v_t in the x_1 direction are [Matthews1977]

$$u_1 = C[\exp(kb_1 x_3) - A\exp(kb_2 x_3)]\exp ik(x_1 - vt)$$

$$u_3 = -ikb_1 C[\exp(kb_1 x_3) - A^{-1}\exp(kb_2 x_3)]\exp ik(x_1 - vt) \qquad (2.4.1)$$

in which $b_1 = [1-(v/v_t)^2]^{1/2}$, $b_2 = [1-(v/v_t)^2]^{1/2}$, and $A = (b_1 b_2)^{1/2}$ are all positive real values, and C is an arbitrary constant depends on the excitation.

Because the two square brackets of Eq. 2.4.1 are real, the longitudinal u_1 and vertical u_3 displacement components are in phase quadrature for each value of x_3.

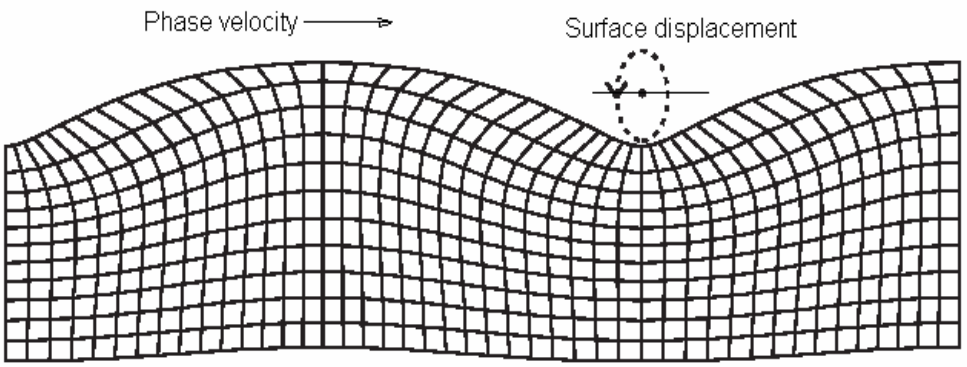

Fig. 2.4.1. *Distortion of a square grid in the sagittal plane by a Rayleigh wave [Matthews 1977].*

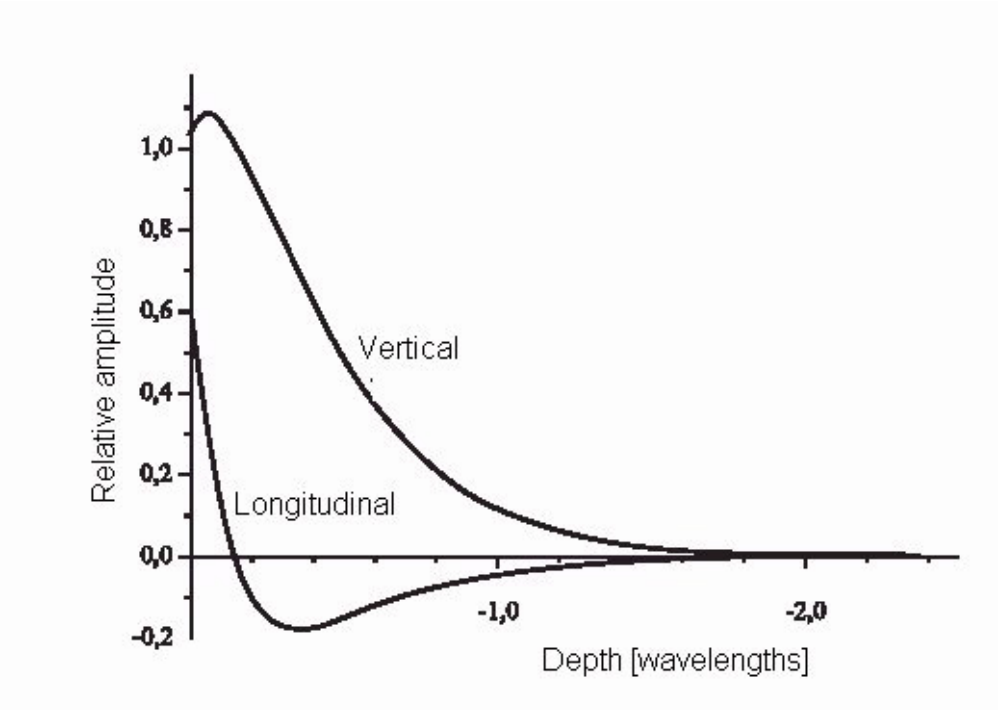

Fig. 2.4.2. *Displacement components of a Rayleigh wave on an isotropic substrate[Mason1970].*

Fig. 2.4.2 shows the depth dependence of the factors multiplying the propagation term in Eq. 2.4.1.

The displacement amplitudes exist only in a region that extends a few wavelengths from the surface.

The basic equations of state that govern the propagation contain the so called "elastic" and "electrical" equations. The first one is the Hook's law, extended by additional stress *eE* due to the piezoelectric effect, and the second one includes electrical polarization *eS*, produced by the strain, *S* [Wixforth1989]. In one-dimensional form these equations can be written as following:

$$T = cS - eE \quad \text{and} \quad D = eS + \varepsilon_0 E \tag{2.4.2}$$

where *T* and *D* is the mechanical stress and the electrical displacement, respectively, which are both linked with mechanical strain *S* and electric field *E*; "*c*" is the stiffness constant and "*e*" is the piezoelectric constant, and ε is the dielectric permittivity. Electrical boundary conditions at the surface of a substrate, on which a SAW is propagating, profoundly influence the propagation parameters (i.e. attenuation and sound velocity of the SAW itself [Wixforth2000]. There are two limiting cases: the so called "open" and "shorten" boundary conditions of the substrate, which depend on the conductivity of a thin layer on the top of the substrate. V_2O_3 with a MIT at T ~ 160 - 170 K provides a possibility to realize both "open", being in isolating state for T < 160 K, and "shorten" (metal for T > 160 K) boundary conditions for propagation of SAW. Thus, this gives a possibility to investigate the elastical and electrical changes in V_2O_3 thin films at the MIT. In compliance with the theory of Ingebrigtsen [Ingebrigtsen 1970], which is valid if the film thickness *d* is small compared to the acoustic wavelength, i.e. $kd << 1$, with $k = 2\pi/\lambda$ the wave number of the SAW, a conductivity dependent attenuation Γ can be written as [Müller2005]

$$\Gamma = K^2 \cdot \frac{\pi}{\lambda} \cdot \frac{\sigma_\square / \sigma_m}{1 + (\sigma_\square / \sigma_m)^2} \tag{2.4.3}$$

Here, K^2 is the electromechanical coupling constant and λ the wavelength of the SAW. The sheet conductance of the film is $\sigma_{\square}$ = (L/w) R^{-1} and $\sigma_m = v_0(\varepsilon_p+\varepsilon_0) = v_0\varepsilon_0(\varepsilon_p/\varepsilon_0 + 1)$ with v_0 the sound velocity of the SAW on a substrate, ε_p is the effective dielectric constant of the piezoelectric and ε_0 the permittivity. The effective dielectric constant is $\varepsilon_p = \varepsilon_0(\varepsilon_{11}\varepsilon_{33} - \varepsilon_{13}^2)^{1/2}$, with ε_{11}, ε_{33}, and ε_{13} the direction dependent dielectric constants of $LiNbO_3$ (tensor elements) at constant stress conditions [Landolt-Börnstein1981].

The normalised sound velocity shift is given by [Müller2005]

$$\frac{\Delta v}{v_0} = \frac{K^2}{2} \cdot \frac{1}{1+(\sigma_{\square}/\sigma_m)^2} \qquad (2.4.4)$$

Here, $\Delta v = v - v_{sc}$, with v_{sc} is the short-circuited sound velocity, introduced in Eq. 2.4.5.

In Fig. 2.4.3 the result for the attenuation Γ and the sound velocity shift, $\frac{\Delta v}{v_0}$, is plotted as a function of the sheet conductivity $\sigma_{\square}$.

For $\sigma_{\square} = \sigma_m$ a maximum attenuation occurs, whereas $\frac{\Delta v}{v_0}$ exhibits a sharp step like increase around this value.

For $\varepsilon_p + \varepsilon_0 = C_s$, with C_s = 5pF/cm for the 128° rotated YX cut of $LiNbO_3$, yielding $\sigma_m = 2\cdot10^{-6}\ \Omega^{-1}$. The absorption coefficient Γ becomes maximal for $\sigma_{\square}=\sigma_m$ resulting in $\Gamma(\sigma_m) = K^2\cdot\pi/2\lambda$ [Müller2005].

In case the surface of the SAW device is covered by a thin metal film, which short-circuits the electric field of the SAW, the piezoelectric material becomes softer due to the missing restoring electrical forces.

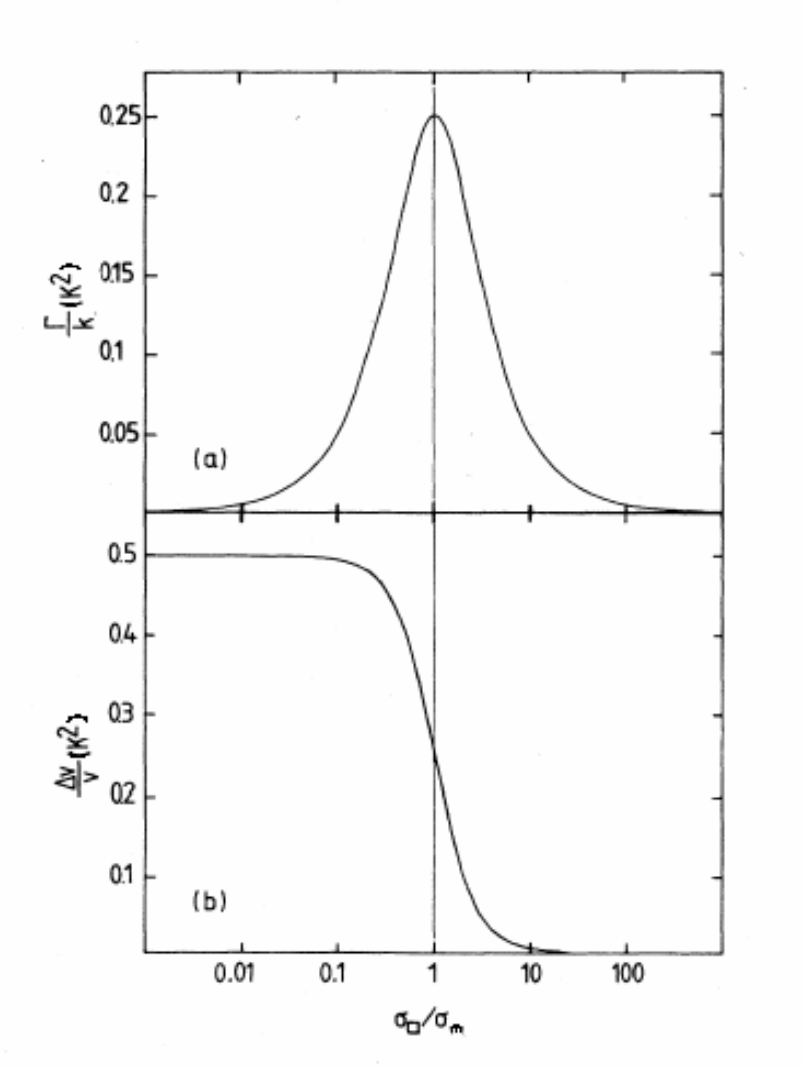

Fig. 2.4.3. *Attenuation (a) and change of velocity (b) for a SAW on a thin conductive layer deposited on a piezoelectric substrate [Wixforth1989].*

The short-circuited sound velocity, v_{sc}, the open sound velocity v_0 and the electromechanical coupling constant K^2 are related by [Matthews1977]

$$v_{sc} = v_0(1 - K^2/2) \tag{2.4.5}$$

This yields the normalized sound velocity shift

$$(v_o - v_{sc})/v_0 = K^2/2 = 0.028 \tag{2.4.6}$$

3. Experiment

3.1 Thin Film Growth

3.1.1 Experimental Setup

The evaporation of thin films with controlled properties requires an operating environment which interferes as little as possible the process of film formation. To minimize the interaction between residual gases and the surface of the growing film, the whole process should be done under very high or ultrahigh vacuum (UHV).

Vacuum system

The presence of impurities in a vacuum system is a serious problem for thin film preparations and studies. The main sources of contamination are contaminants brought into the system on the substrate surface, residual contaminant gases or vapors in the vacuum system, and gases released from the source material or the heater material. An important effect of contamination is the loss of adequate adherence of the deposited film. Contamination in the form of gaseous impurities can be minimized or eliminated by the use of an UHV system.

Fig. 3.1.1.1 shows a schematic view of the experimental UHV chamber used for the present work which includes several main parts:

- The vacuum system

  - stainless-steel growth chamber (all the components of the growth chamber must be able to resist bake-out temperatures of up to 160°C for extended periods of time, which are necessary to minimize outgassing from the internal walls)

  - load-lock module for transfer to and from air, and where substrates are degassed prior to growth.

- The pumping system

  - two turbomolecular pumps (one for load module, and one for growth chamber); basic pressure in the chamber ~ 10^{-8} mbar

- Sample heater (electron beam) up to 1200° C.
- The sample holder manipulator which is capable of continuous rotation around its axis.

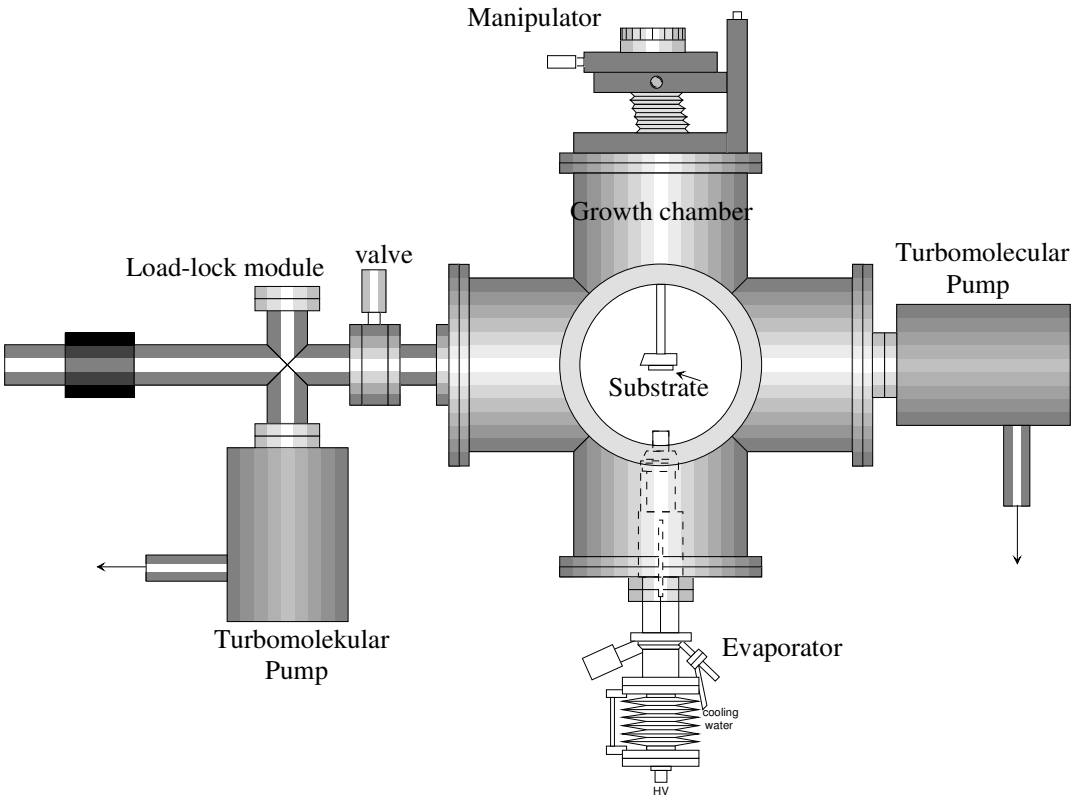

Fig. 3.1.1.1. *Schematic view UHV chamber.*

Evaporator

In the present work an electron beam evaporator (UHV-evaporator EFM3 Omicron) was used (Fig. 3.1.1.2). In this UHV evaporator the material is evaporated from a bar (target) by electron bombardment heating. The bombarding electron beam induces a temperature rise of the evaporant, causing evaporation.

The beam exit column contains an ion collector which serves as a flux monitor. At a given electron emission current (I_{em} ~ 700 nA in the present work) and e-beam energy the ion flux measured there is directly proportional to the flux of evaporated atoms. The ion is displayed on the indicator of the electronics unit.

The evaporator has a shutter at its outlet which can be opened and closed by a rotary drive. This allows precise flux adjustment prior to exposure, and exact control of the evaporation time.

The evaporation cell is contained in a water-cooled copper cylinder (cooling shroud). This and the fact that just a restricted region of the evaporant is heated facilitates to keep the background pressure during evaporation below 10^{-7} mbar.

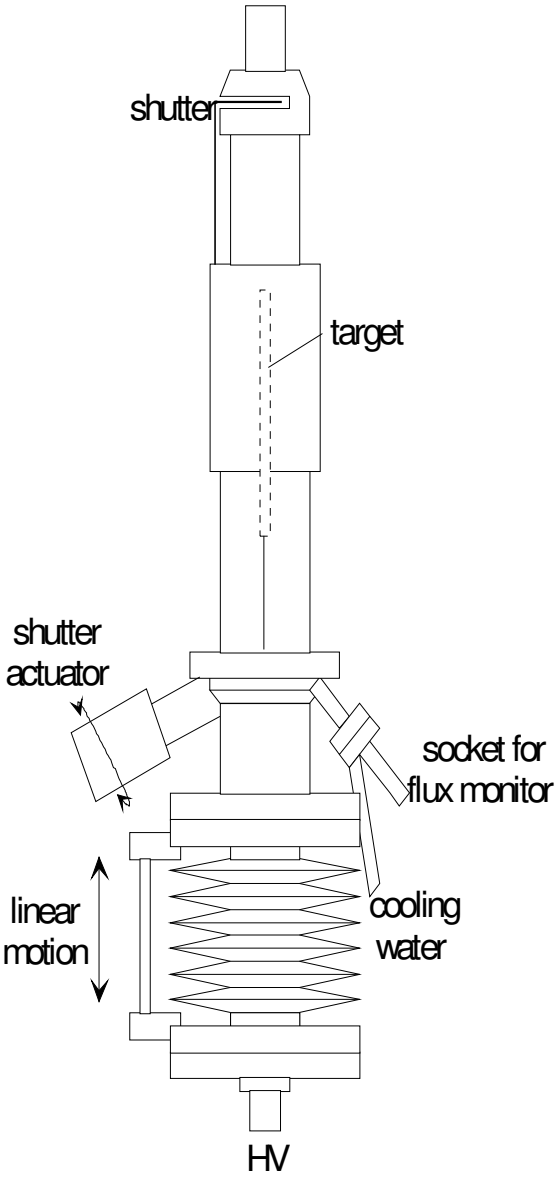

Fig. 3.1.1.2. *Schematic view of UHV evaporator.*

Furnace

For target preparation and also for annealing treatments of grown V_2O_3 thin films (which will be described later on) the furnace HTM LORA was used (Fig. 3.1.1.3). Originally designed as laboratory furnace for reducing atmospheres, the LORA furnace has been developed into versatile laboratory tube furnace for oxidizing, reducing and inert atmospheres.

The heater (Mo wire) is directly wound onto the surface of the work tube (not shown here). Permanent flushing of the heater room with protective gas prevents the heater coming into contact with oxygen. For this reason the furnace is specifically suited for work at highest temperatures.

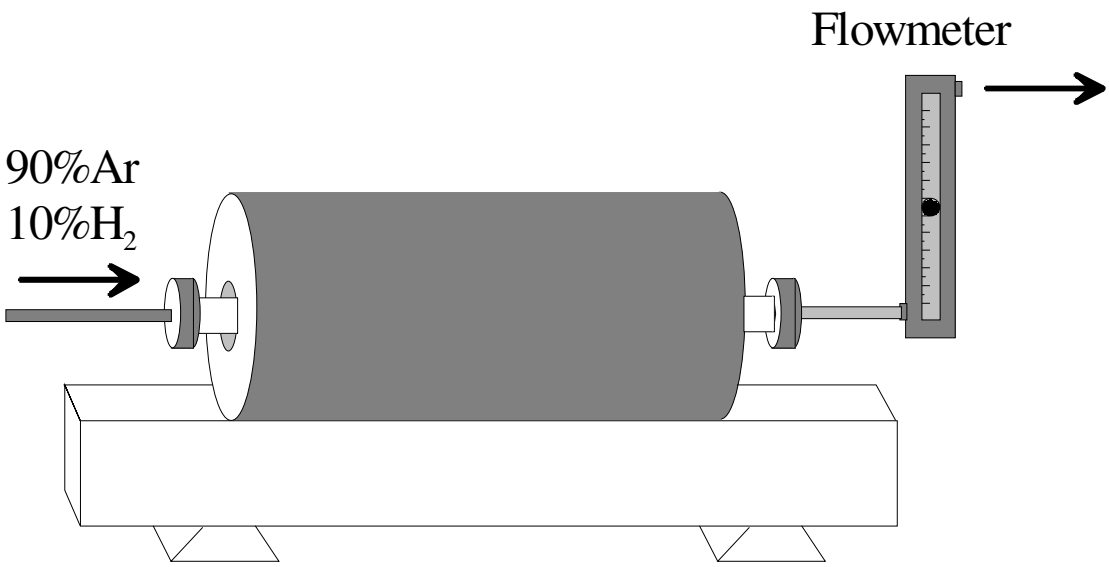

Fig. 3.1.1.3. *View of HTM LORA furnace with flowmeter controller.*

The temperature profile shown in Fig. 3.1.1.4 indicates that the temperature inside the furnace around its center is constant over a distance of more than 7 cm.

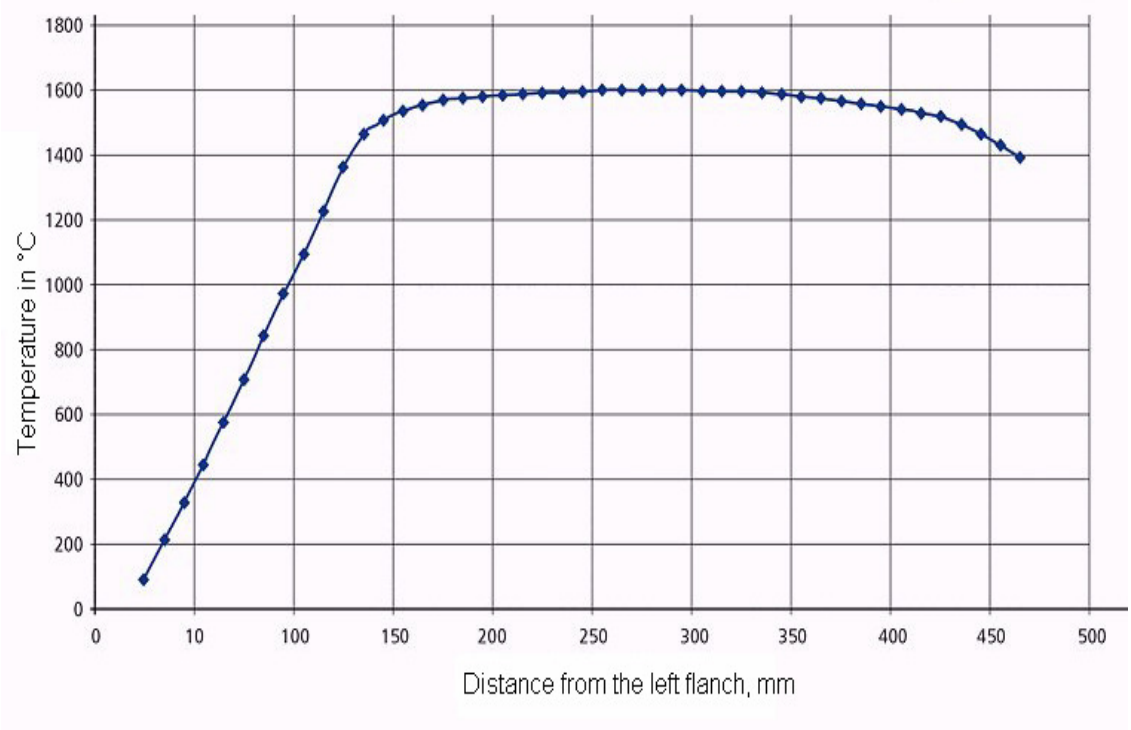

Fig. 3.1.1.4. *Temperature profile of the furnace (HTM LORA)*

The working flow rate of gas mixture 90%Ar+10%H_2 is controlled by a flowmeter which is mounted at the outlet of the tube.

3.1.2 Target Preparation

Before pressing the target, Vanadium(III) oxide (99,9%) powder was ground in an agate mortar to obtain fine particles. To exclude humidity, ground material was dried at 150°C in an evacuated quartz ampoule for 6 hours while it was continuously pumped to a pressure ~ 10^{-5} mbar.

The next step was to press the target with a force of approximately 6 tons (Fig 3.1.2.1).

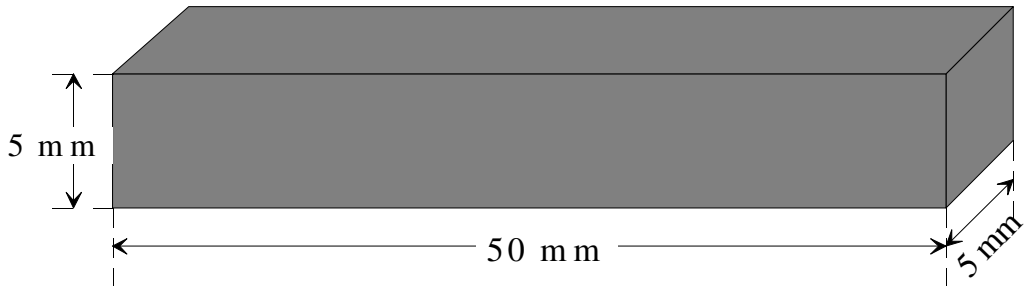

Fig. 3.1.2.1. *Schematic view of V_2O_3 pressed target.*

The pressed target was sintered in the furnace (see Chapter 3.1.1) under reducing atmosphere (90%Ar + 10%H_2) at 850°C for 8 hours. Afterwards it was characterized by X-ray Diffraction (XRD) and resistivity measurements.

XRD measurements on powdered samples was carried out in the Θ/2Θ mode with 2Θ ranging from 10° to 75° (Fig. 3.1.2.2).

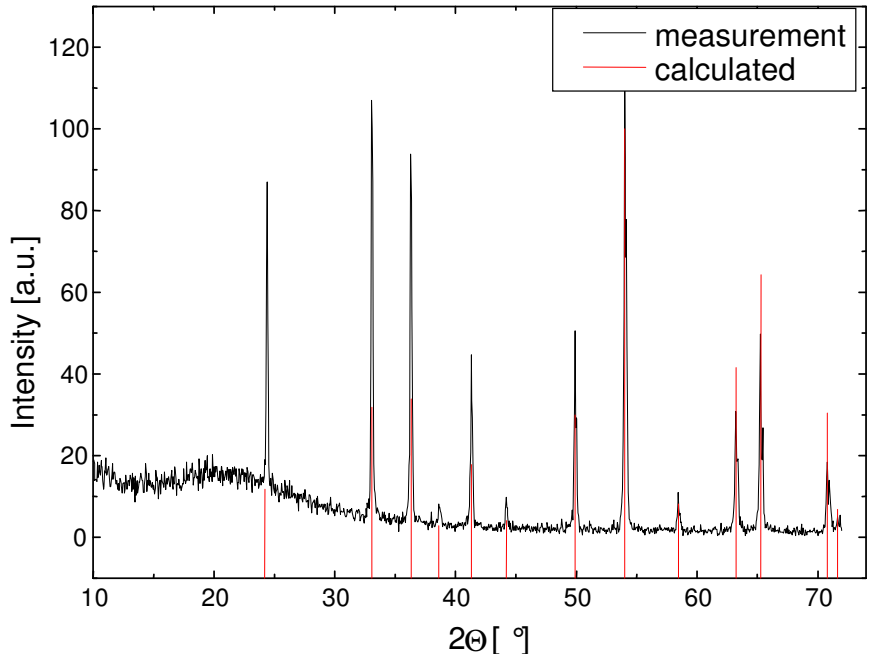

Fig. 3.1.2.2. X-*ray diffraction measurement of a powdered V_2O_3 target.*

The experimental XRD pattern show good agreement with the calculated data for stoichiometric V_2O_3 compound.

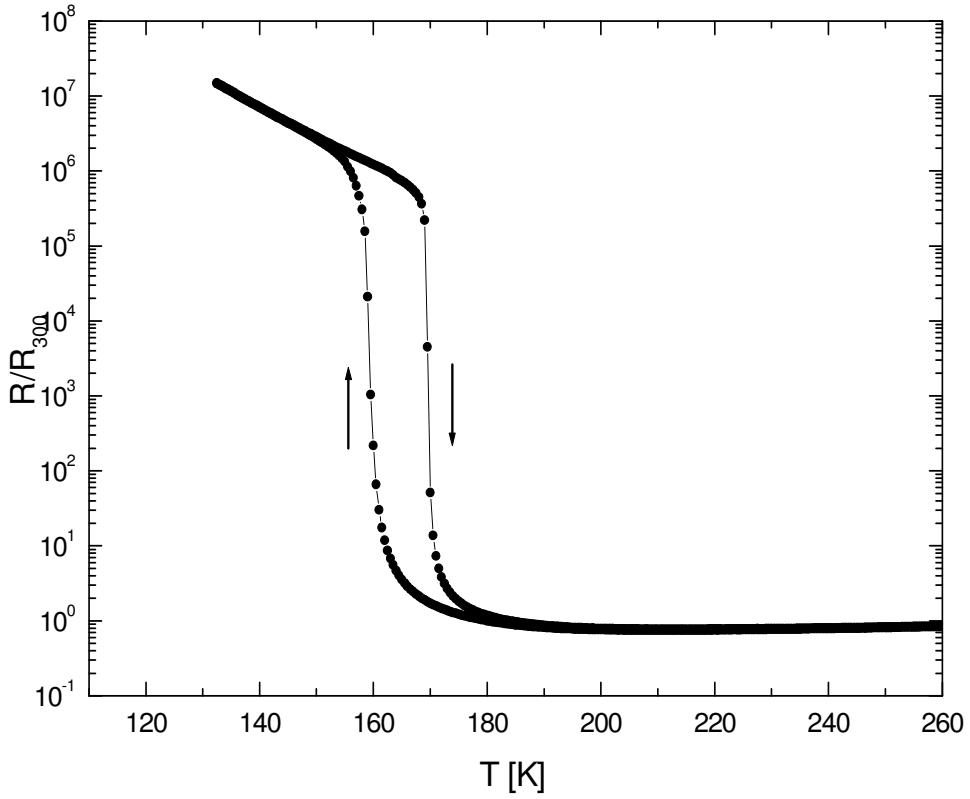

Fig. 3.1.2.3. *Temperature dependence of the resistivity of a V_2O_3 target normalized to room temperature resistivity.*

Additional to XRD measurements all targets were characterized by resistivity measurements (four-point method, see Chapter 3.2.5). A typical measurement is shown in Fig. 3.1.2.3. The resistivity manifests a sharp increase of more then six orders of magnitude at around 170K with a pronounced hysteresis on cooling and warming. The above shown results clearly demonstrate that the target is reflecting intrinsic properties of V_2O_3 of high purity and stoichiometry. Impurities and non-stoichiometry would reduce the transition temperature (see Chapter 2.1.2).

3.1.3 Substrate Preparation

In the present work polycrystalline diamond and $LiNbO_3$ (128° rotated YX cut) substrates were used.

As can be observed from the scanning electron microscopy image of the polycrystalline diamond substrate (Fig. 3.1.3.1), the grain size of this substrate is between 5 - 10 μm.

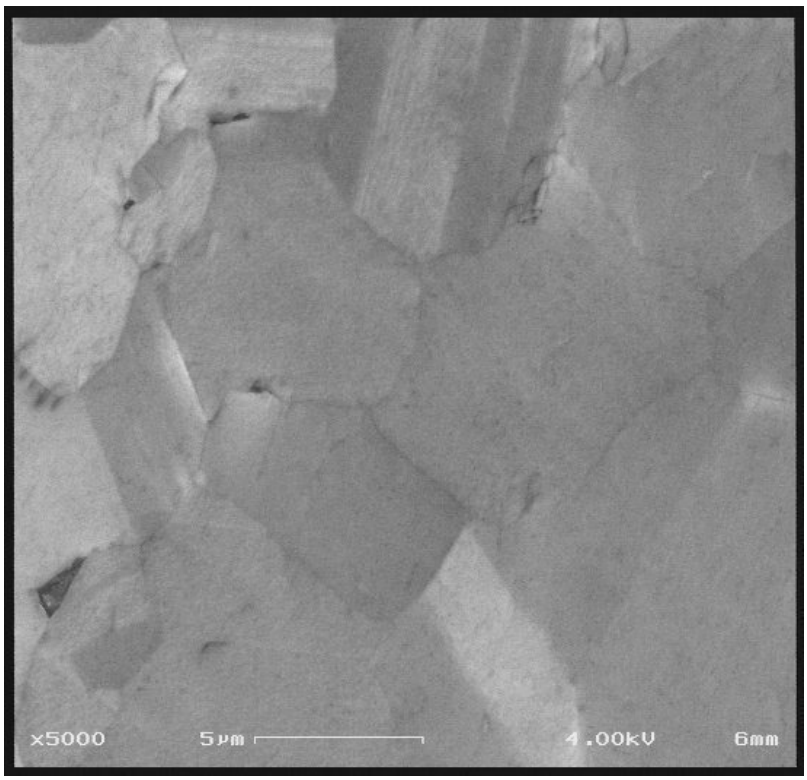

Fig. 3.1.3.1. *Scanning electron microscopy image of diamond substrate.*

Fig 3.1.3.2 shows a schematic view of $LiNbO_3$ substrate used for deposition of V_2O_3 thin films in SAW study. On the top of the substrate two IDTs are deposited by electron beam evaporation method.

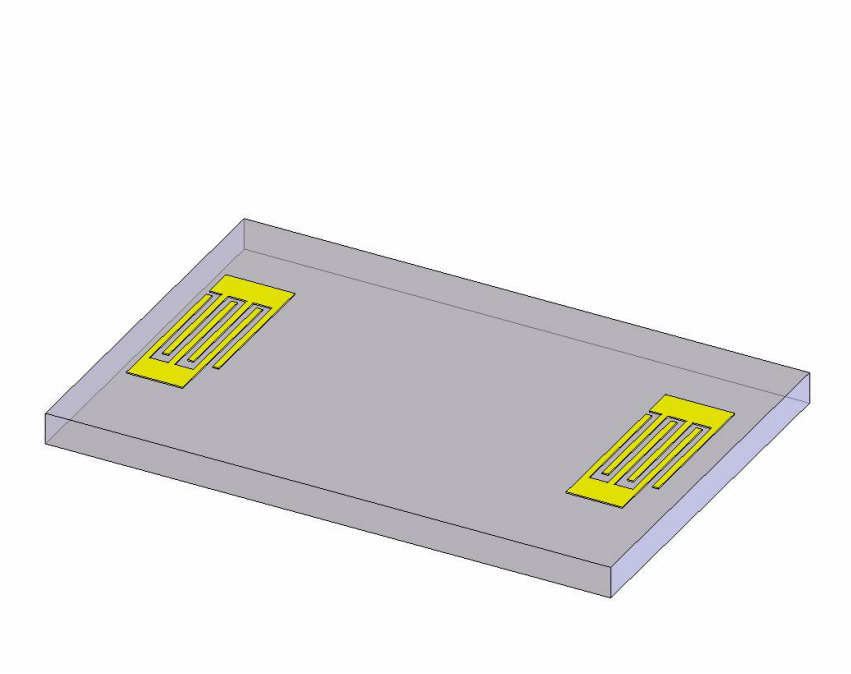

Fig. 3.1.3.2. *Schematic view of $LiNbO_3$ substrate [Hörner2005].*

In studies of the growth of thin films, the substrate surface is of critical importance, since the surface plays a major role in the growth processes. Ideally, the surface should be extremely flat, smooth, and free of crystalline defects. It should be also free of chemical impurities.

The cleanliness of the substrate surface exerts a decisive influence on the film growth and adhesion. A thoroughly cleaned substrate is a prerequisite for the preparation of film with reproducible properties. The choice of cleaning techniques depends on the nature of the substrate, the type of contaminants and the degree of cleanliness required.

First step for all substrates was a cleaning in acetone and methanol in ultra sonic bath for 30 min to remove grease from the surface. Then all dry substrates were glued on a molybdenum sample holder using a suspension containing liquid graphite (Fig. 3.1.3.3), which also improves the thermal contact. Afterwards the sample holder was introduced into a load-lock chamber (see Chapter 3.1.1).

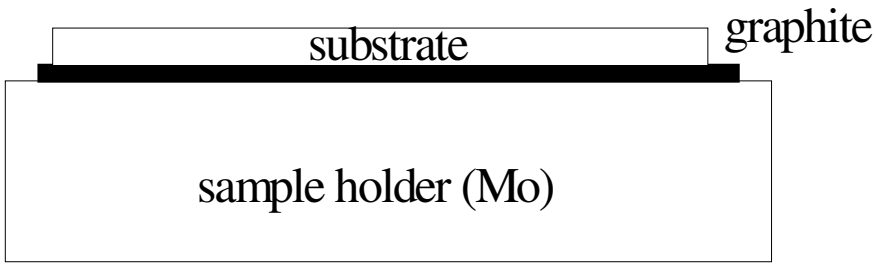

Fig. 3.1.3.3. *Schematic view of a substrate glued on a sample holder.*

From the load-lock chamber the sample holder was transferred into the UHV chamber (Fig. 3.1.1.1) followed by a continuous pumping procedure. The second step of the cleaning includes heating the substrate inside the main chamber to a temperature of 900°C for diamond and 120°C for $LiNbO_3$ substrates, respectively, for usually 2 - 3 hours. The temperature was controlled by a thermocouple on the sample holder at temperatures below 300°C and by a pyrometer at higher temperature range. Before deposition, substrates were cooled down to room temperature.

3.1.4 Deposition and Annealing

To reach reasonable evaporating rates a temperature around 1800°C (for V_2O_3 target) would be necessary. Using the UHV-evaporator EFM3 Omicron (see Chapter 3.1.1), V_2O_3 was evaporated from the sintered target (see Chapter 3.1.2) and deposited on the substrate. The substrate temperature during the deposition process was kept at a constant value of 300 K. In the following table basic parameters of deposition are presented.

Distance from evaporator to substrate (cm)	Working pressure (mbar)	Substrate temperature (K)	Deposition Rate (Å/min)
30	10^{-7}	300	10

Table 3.1.4. *Working parameters of deposition.*

The film thicknesses were determined *ex situ* by a Dektak profilometer. Typical thickness of thin films prepared in this work were $d \sim 260$ nm.

The conventional technologies utilize growth of V_2O_3 thin films on a substrate at high temperature (600°C). However, due to the large mismatch between V_2O_3 and the diamond substrate, attempts to grow thin films on the diamond substrate by using this method were not successful. In particular the resistivity jump indicating the MI transition was not observed for such films. The attempt to grow V_2O_3 thin films on the $LiNbO_3$ substrate was not successful as well, because of the very high diffusion of Li into bulk V_2O_3, especially at such high substrate temperatures.

Taking into consideration above mentioned limitations, in course of the present work another technological process was developed.

Thus, after deposition at room temperature the thin films were tempered in reducing atmosphere (90%Ar + 10%H_2) for 80 hours, at different temperatures (300 - 450°C) in the furnace (see Chapter 3.1.1). By this reduction annealing it was possible to equilibrate the composition of the grown thin films with approaches to stoichiometry. One of the main advantages of this method consists in using an annealing temperature of 450°C, which is considerably reduced compared to conventional methods of V_2O_3 thin film growth.

The typical temperature regime used for thermal treatment is presented on Fig. 3.1.4.

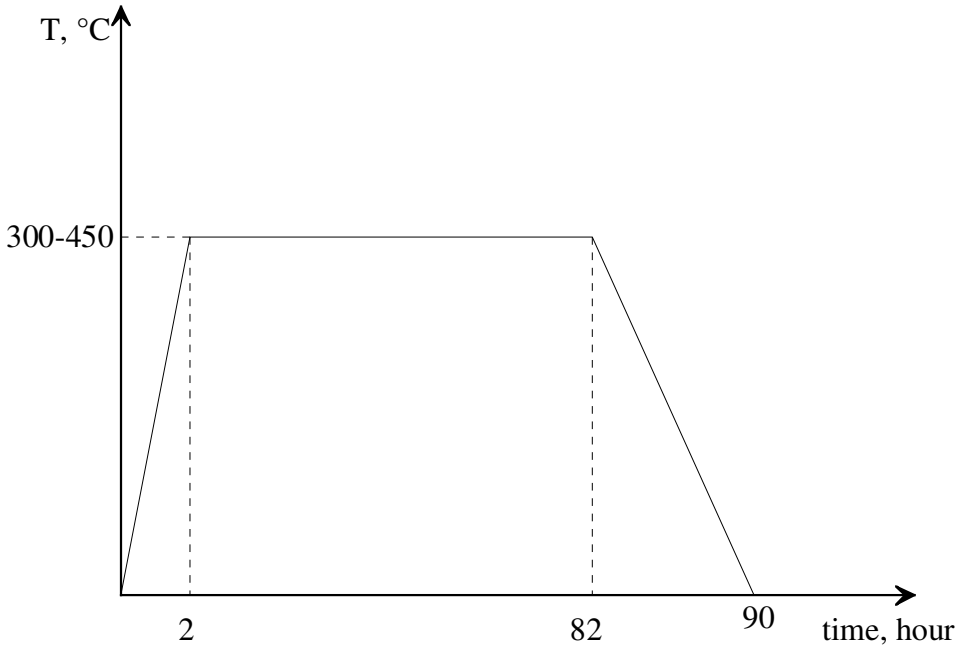

Fig. 3.1.4. *The typical temperature regime.*

Samples were heated at a constant rate up to temperatures between 300 and 450°C during two hours. The temperature was kept constant during 80 hours with the following cooling to room temperature for 8 hours.

3.2 Characterization Techniques

3.2.1 Dynamic Secondary Ion Mass Spectrometry (SIMS)

Dynamic secondary ion mass spectrometry (SIMS) measurements were performed using an ATOMIKA 4100 secondary ion mass spectrometer. High resolution depth profiles of the thin film composition were measured with a scanned and focused Cs^+ primary sputter ion beam at an energy of 5 keV and a sputter angle of 45° (Fig. 3.2.1). The ion beam was scanned over an area of 200x300 µm². An electronic gating was applied in order to exclude secondary ions sputtered from the crater edge. Diatomic secondary ions MCs^+ with M = V, O were detected for depth profiling in order to minimize matrix effects especially in the near vicinity of the V_2O_3-substrate interface.

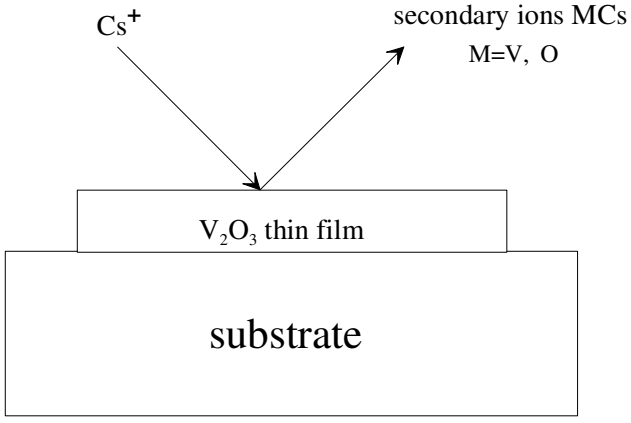

Fig. 3.2.1. *Schematic view of the secondary ion sputtering used for SIMS measurements.*

3.2.2 Rutherford Backscattering Spectrometry (RBS)

To measure the stoichiometry of thin films RBS has been used. It relies on the fact that the energy of an elastically backscattered particle depends on the mass of the target atom (kinematic factor) and on the depth at which the scattering took place (energy loss on the way to and from the point of interaction). This allows to profile the elemental composition of the sample close to the surface. The RBS is suited best for the detection of heavy elements on light substrates (sensitivities between 10 and 10^{-4} monolayers can be reached).

The measurements were performed with 3.5 MeV He^{++} ions delivered by a tandem accelerator. The backscattered ions were detected under an angle of 170° with respect to the incident beam by a semiconductor detector (silicon surface barrier detector). The spectra were simulated using the RUMP computer program. The accuracy of the results is of the order of 1%.

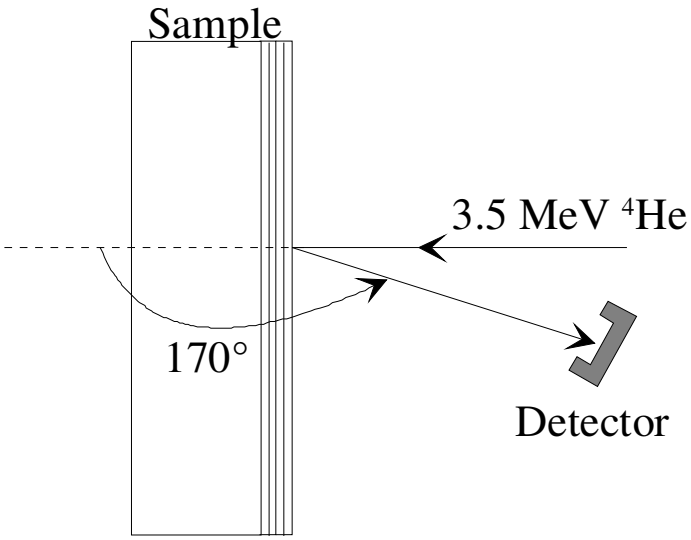

Fig. 3.2.2. *Experimental setup for Rutherford backscattering spectrometry.*

The ions penetrate the sample, interact with the atomic nuclei and travel back out. During this process the ions lose energy by scattering on the nuclei in the sample. A part of the scattered ions are collected in the detector.

The signal from an atom at the sample surface will appear in the energy spectrum at a position $E_1 = kE_0$. The signal from atoms of the same mass below the sample surface will be shifted by the amount of energy lost while the projectiles pass through the sample, before (ΔE_{in}) and after collision (ΔE_{out}).

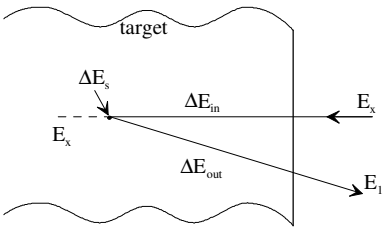

$$\Delta E_{in} = \left(\frac{dE}{dx}\right)_{in} * \Delta x$$

$$\Delta E_s = (1-k) * E_x \quad \text{(kinem. loss)}$$

$$\Delta E_{out} = \left(\frac{dE}{dx}\right) * \frac{\Delta x}{\cos\Theta}$$

Detected energy: $E_1 = E_0 - \Delta E_{in} - \Delta E_s - \Delta E_{out}$

3.2.3 X-ray Diffraction (XRD)

Bragg-Brentano X-ray diffraction setup

The most prominent applications of X-ray powder diffraction are: identification of single-phase materials, identification of multiple phases in microcrystalline mixtures or determination of the crystal structure of identified materials. In Fig. 3.2.3.1 the schematic view of XRD measurement arrangement is presented.

The incident beam interacts with the target material and one of the primary effects that can be observed is the scattering of these X-rays from atomic scattering centers within the target material.

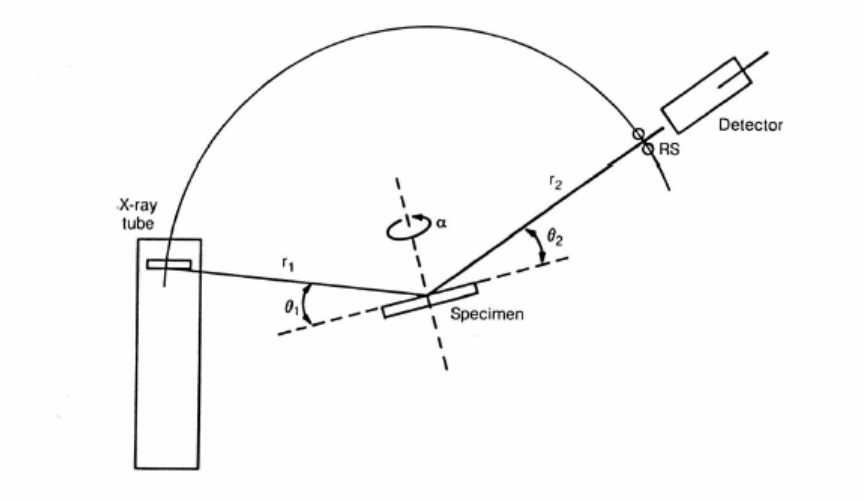

Fig.3.2.3.1. *Schematic view of XRD measurement arrangement.*

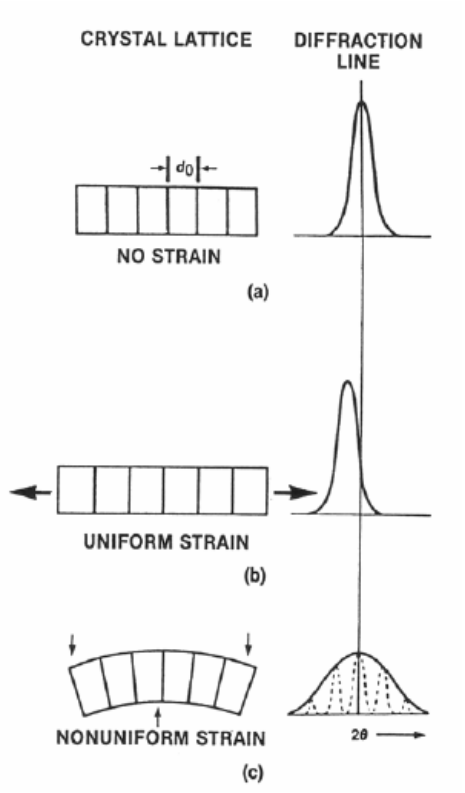

Fig. 3.2.3.2. *Strain expanding and contracting d-values [Jenkins1996]*

If the material has some type of crystalline structure, X-rays scattered in certain directions will be amplified, while most will be out of phase (diffraction process). Using measurements of the Bragg-Brentano geometry, one can discern the crystal structure and the unit cell dimensions of the investigated material and the intensities of the amplified X-ray can give the information about arrangement of atoms in the unit cell.

If material contents strain (Fig. 3.2.3.2) it can produce two types of diffraction effects. In case so called macrostrain (uniform strain) the unit cell dimensions become either larger or smaller and resulting in a shift of the diffraction peaks in the pattern. (Fig. 3.2.3.2(b).

Macrostrain causes the lattice parameters to change in permanent manner resulting in a peak shift. A distribution of tensile and compressive forces produces microstrains and results in a broadening of the diffraction peaks (Fig. 3.2.3.2(c) Microstrains can be produced by dislocations, vacancies, shear plain, etc.

Guinier X-ray Diffractometry Setup

For X-ray measurements on V_2O_3 thin films deposited on diamond substrate a „Guinier Thin Layer Diffractometer“ was used. Here basically the Debye-Scherrer-Method is used together with a characteristic double focused alignment (Fig. 3.2.3.3). Point f_1 holds a punctiform X-ray source. A monochromator selects Cu-Kα - radiation which meets the sample afterwards and gets diffracted. A scintillation counter records the spectrum of the diffracted radiation.

A special feature of the Guinier Diffractometer is the small angle of incidence (Ψ is between 1° and 10°). Therefore the intensity of the beam is maximized directly on the surface of the specimen which is advantageous in thin layer analysis.

As can be seen in the figure, x-ray source and monochromator are located on a circle with radius $2rF_1$. As can be shown with the *Sehnensatz,* diffracted beams intersect again so that a focalization is reached.

The monochromators point of focalization is also located on the detectors circle. So the analogue arrangement of point of focalization, detector and specimen leads to focalization as well. The specimen is not curved. But the corresponding error can be neglected due to the beams small mark.

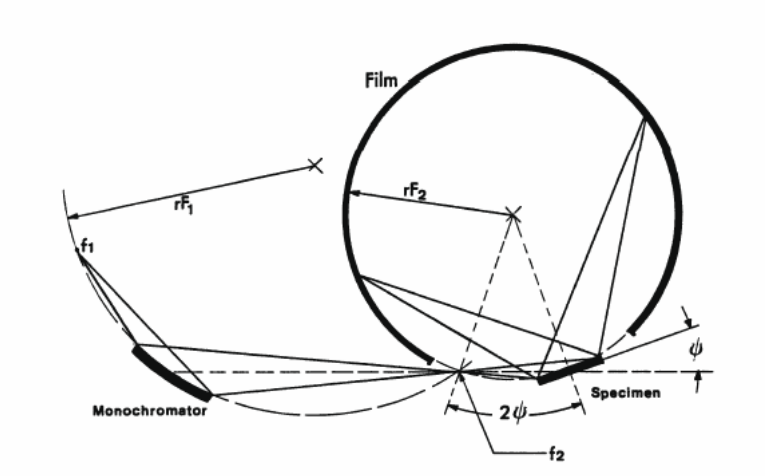

Fig. 3.2.3.3. *Principle of focalization in Guinier's setup*
In point f1 the punctiform x-ray source is located. The detector moves along the circle with radius rF2.

3.2.4 Atomic Force Microscopy (AFM)

Atomic force microscopy (AFM) is a powerful technique for imaging surfaces down to the sub-nanometer level (without additional sample preparation).

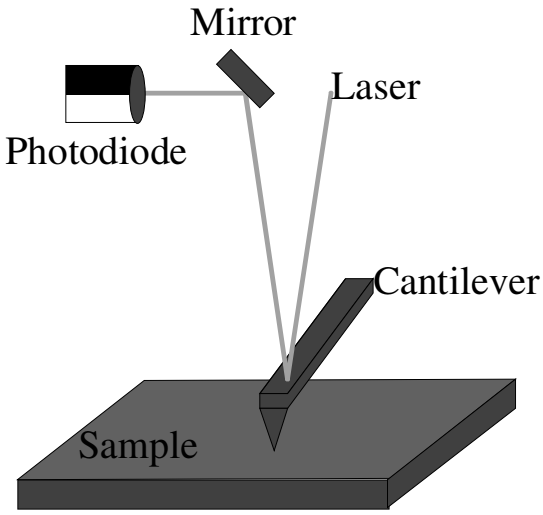

Fig. 3.2.4.1. *Experimental setup for atomic force microscopy.*

The AFM consists of a sharp tip (10 - 20 nm diameter) attached to a stiff cantilever (Fig. 2.3.4.1). This tip is brought close to the surface and the sample is scanned beneath the tip. The tip moves in response to tip-surface interactions. And this movement is measured by focusing a laser beam onto the back of the cantilever and detecting the position of the reflected beam by a photodiode.

The atomic force microscope is operated in two basic modes: contact and tapping. In the contact mode the AFM tip is in contact continuous with the surface, whereas in the tapping mode (also called intermittent contact mode) (Fig. 3.2.4.2) the AFM cantilever is vibrated above the sample surface, so that the tip is only in contact with the surface intermittently. This helps to reduce shear forces associated with the tip movement. For most imaging in the AFM, the tapping mode is the recommended mode. Contact mode AFM is only used for specific applications, such as force curve measurements.

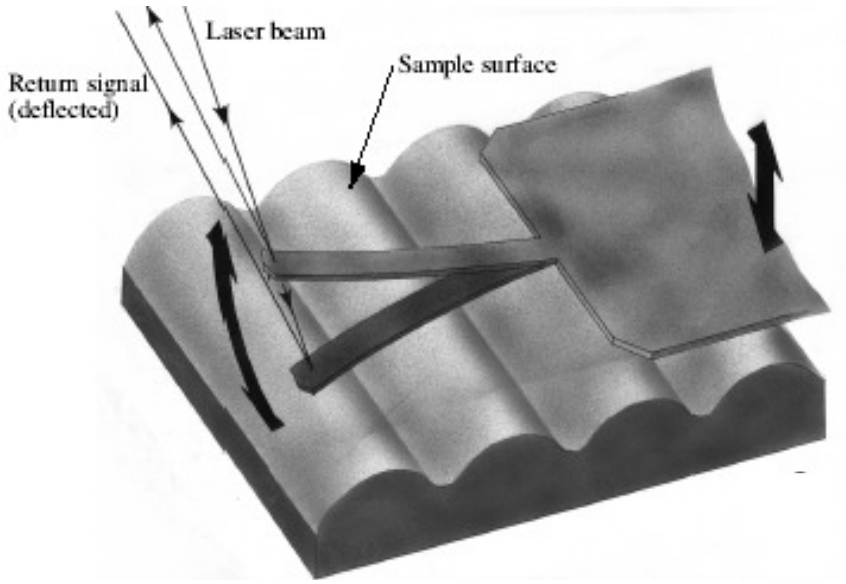

Fig. 3.2.4.2. *Tapping cantilever on the sample surface.*
(The optical level technique reflects a laser beam off the back of the oscillating cantilever, these to a segmented photodiode. The differential signal between the top and bottom photodiode segments provides a sensitive measure of cantilever deflection).

3.2.5 Resistivity Measurements

Electrical resistivity of the V_2O_3 thin films was measured by a standard four probe technique. This method eliminates the resistance of contacts and wires, which is important at high temperatures where the sample (V_2O_3) is metallic and the total resistance is rather low (a few Ohm).

A DC method was used with automatic reverse of polarity to eliminate offset voltages, like thermopower. A voltage excitation of typically 3 V (or below) and a shunt resistance (1 kOhm) restricts the maximum current through the sample below 3 mA. For current measurement and voltage measurement (sample) a Keithley-6517A and nanovoltmeter Keithley-182 were used, respectively. Temperature dependent measurements were performed in a home built cryostat down to a temperature of ~ 80 K or ~ 6 K using liquid Nitrogen or liquid Helium cooling agent, respectively. The maximum resistivity that could be measured by this setup was of the order of 10^8 Ohm (at temperatures below the metal to insulator transition (T_{MIT})).

Bond contacts for the DC measurements of V_2O_3 deposited on $LiNbO_3$ substrate (Al wires, diameter 50 μm) were placed near the edge of the film. The current leads were fixed at ~ 1.5 mm and ~ 1 mm from the left and right corner, respectively. The voltage probes (distance L = 320 μm, midpoint to midpoint) were placed approximately in the middle between the current leads.

Fig. 3.2.5 shows a typical behavior of the temperature dependence of resistivity of V_2O_3 thin film.

The width of the transition (ΔT_{MIT}) together with the transition temperature (T_{MIT}) and the resistivity jump are characteristics for the metal to insulator transition (MIT). For thin films MIT is broader and the transition temperature is lower compared to the bulk material. The ΔT_{MIT} is defined by the points on interception of the extrapolated resistivity curves below and above the transition with the line drown through the steepest slope of the R(T) curve. The temperature of the transition T_{MIT} is defined as a midpoint of the resistivity jump.

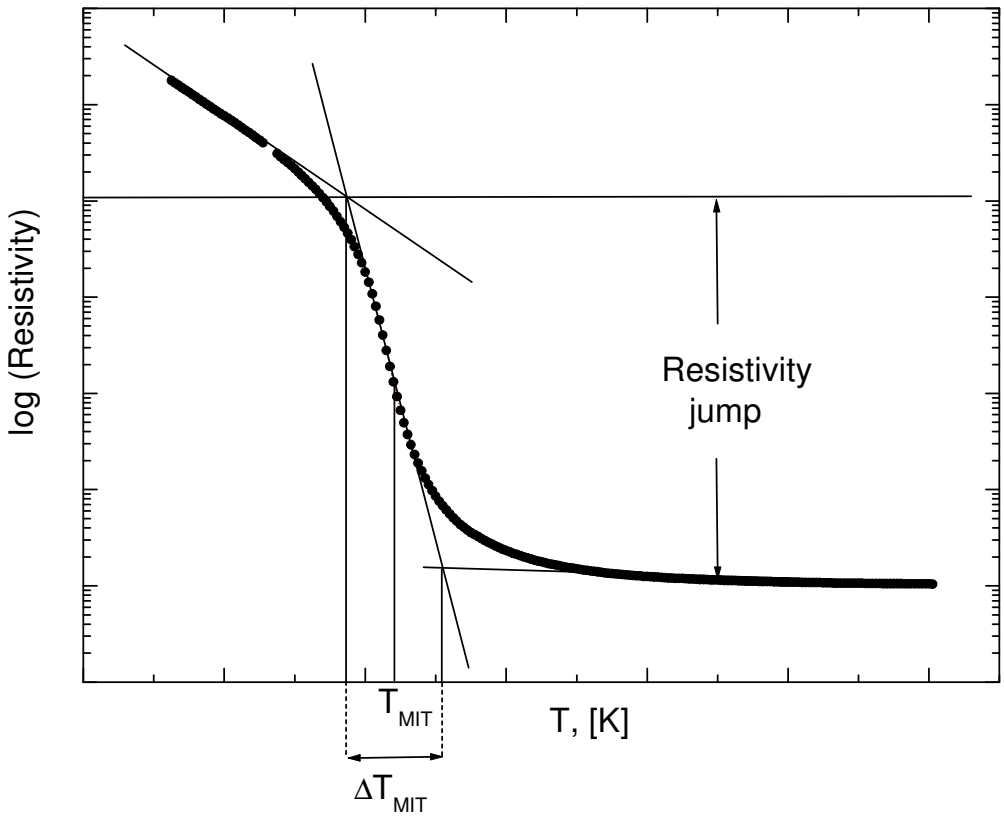

Fig. 3.2.5. *Typical temperature dependence of resistivity for V_2O_3*

3.2.6 Surface Acoustic Waves (SAW) Experiments

To excite and measure the sound velocity and attenuation of surface acoustic waves, interdigital-transducers (IDTs) with split-4-finger electrodes were used. In Fig. 3.2.6 schematic view of a surface acoustic transmission line is presented.

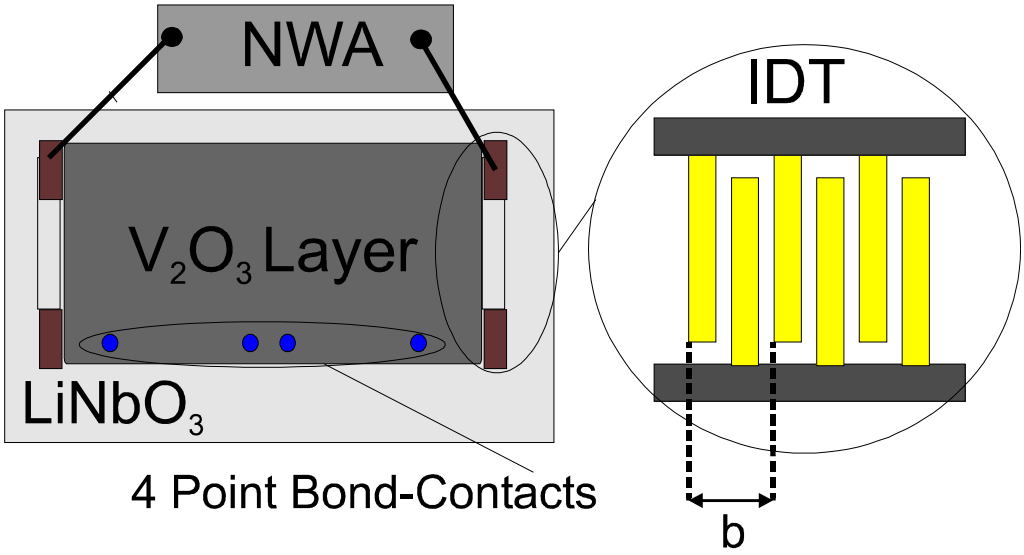

Fig. 3.2.6. *Schematic view of a surface acoustic transmission line. (V_2O_3 film on top of $LiNbO_3$ together with an enlarged view of the IDT structure. Bond contacts serve for dc resistivity measurements.)*

On top of a piezoelectric substrate ($LiNbO_3$ with a 128° rotated YX cut) the IDTs were positioned, i.e. a propagation of the SAW in X direction. These IDTs are centred at ~ w/2 of the V_2O_3 film (L_F = 4.18 mm and w = 2.7 mm is the length and width of V_2O_3 thin film respectively). The fingers of the electrodes extend over about 25% of the width. The distance between the right and left IDTs and the film is ~ 0.35 mm and ~ 0.47 mm, respectively.

To excite the SAW, a radio frequency voltage with the fundamental frequency of the IDT (typically 112 MHz) was supplied to one of the IDTs

The SAW is emitted by one of the interdigital-transducers and propagates along the substrate from the sending IDT to the identical receiving IDT, where it is detected electrically. The propagated SAW has an electrical and a mechanical part due to the piezoelectricity of $LiNbO_3$. The wavelength λ of the SAW is defined by the spacing b (see Fig. 3.2.6 inset) of the finger electrodes. Since the distance of the metallic lines in the split-4-finger electrodes (midpoint) is 4.33 µm, λ=8∗4.33 µm = 34.64 µm from the geometry. The best emitted frequency f_0, called the fundamental frequency, is then determined by the sound velocity

$$\lambda \cdot f_0 = v_0 \tag{3.2.6}$$

v_0 = 3978.2 m/s is the sound velocity of 128° rotated YX $LiNbO_3$ at room temperature [Kovacs1990].

The IDT structure behaves like a band pass filter. Therefore, it is essential to measure the attenuation at the frequency f_0, which has the highest transmission. Otherwise, the contribution of attenuation coming from the filter characteristics. To avoid this contribution , the frequency with the lowest attenuation was tracked (in range the 109 - 117 MHz) during the whole measurement and used as the fundamental frequency. The overall attenuation of the applied and detected electrical radiofrequency signal was determined by a vector network analyser "NWA" (ZVC, Rohde and Schwarz)

Additionally, the group velocity was measured with a second independent channel of the NWA. Measurements between 260 K and 4.2 K were performed in a cryostat (American Magnetics) with a variable temperature insert (VTI).

4. Results and Discussion

4.1 V_2O_3 Thin Films Grown on Diamond Substrates

V_2O_3 thin films were successfully grown on diamond substrates using a new growth method described in the previous chapter. Structural and electrical properties of the obtained thin films were studied by different characterization techniques (described in Chapter 3.2). The results of these characterizations are presented in the following chapter.

4.1.1 Resistivity Measurements

To demonstrate the advantage of the new method of the film growth, a comparison with the V_2O_3 thin films grown on diamond by conventional method [Schuler1997] is given.

The temperature dependence of the resistivity normalized to room temperature resitivity (R_{300}) of thin V_2O_3 films grown on diamond substrate by conventional *in situ* growth technique is shown in Fig. 4.1.1.1. In this case, the substrate temperature was kept at 600°C, during the growth, and no subsequent thermal/reducing treatment (see Chapter 3.1.4) was done.

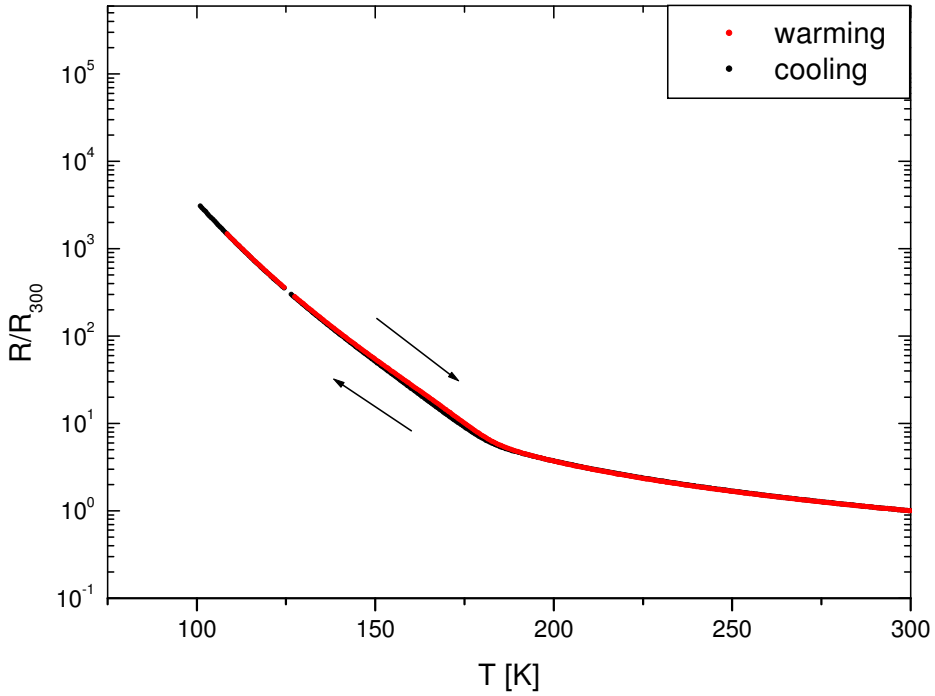

Fig. 4.1.1.1. *Temperature dependence of the resistance of V_2O_3 thin film grown in situ by conventional method.*

The measured thin films do not show a pronounced metal to insulator transition (MIT). In the temperature range 300 - 175 K a semiconducting behavior, dR/dT<0, is seen with the resistivity increase of about one order of magnitude. Below 175 K a stronger increase (more than two orders of magnitude) is observed. Thus, no characteristic feature of MIT can be revealed on such thin films.

The properties of the V_2O_3 thin films prepared by the method developed in the present work drastically differ (see below), compared to the *in situ* grown films. The resistivity of as grown (temperature of the substrate: T_{sub} = 30°C) V_2O_3 thin film, measured directly after the deposition, i.e. without annealing, is shown in Fig. 4.1.1.2. One can hardly see any resistivity jump.

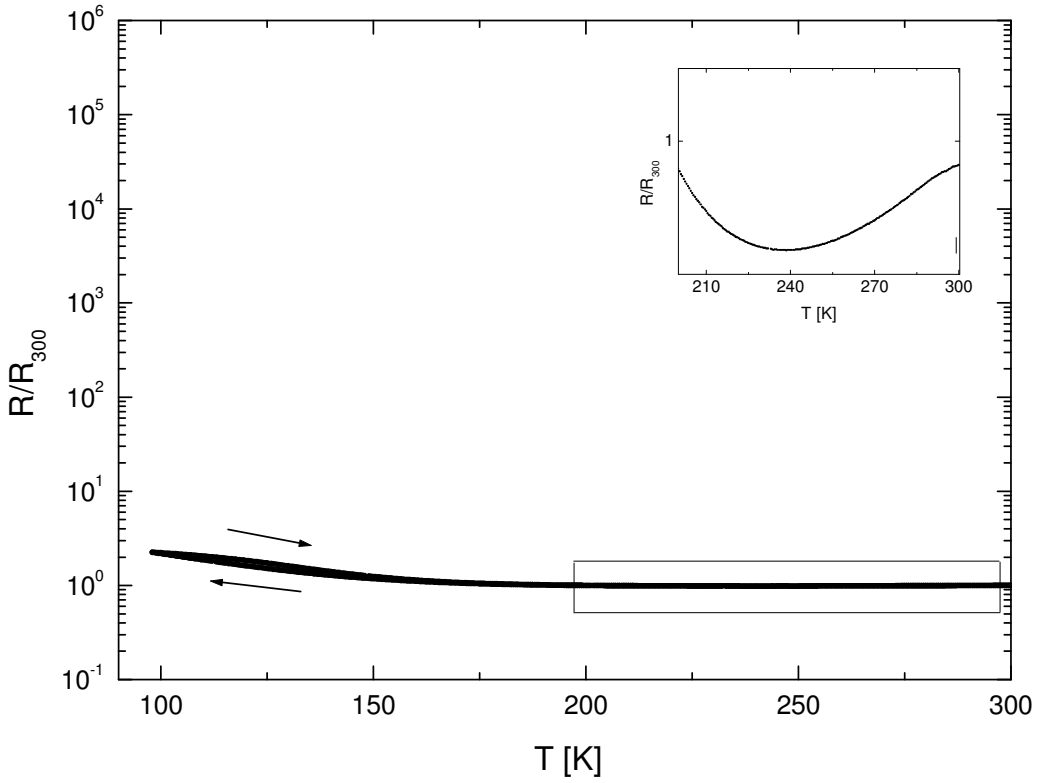

Fig. 4.1.1.2. *Temperature dependence of the resistance of the V_2O_3 thin film grown at low substrate temperature, T_{sub} = 30 °C.*

However, already the as grown film demonstrates a metallic behavior, dR/dT>0, at high temperatures T = 300 - 240 K as one can see in the inset in Fig. 4.1.1.2. This is in clear contrast with conventional in situ grown film on diamond. A possible reason for such resistance behavior is that the film, deposited at such low temperature, possess very small grain size (or even did not crystallize). To improve the crystalline quality of the as grown films and to optimize their electrical properties we performed a subsequent thermal treatment at different temperatures.

Fig. 4.1.1.3 - 4.1.1.6 show the temperature dependencies of resistivity of thin films after annealing at 300, 360, 400, and 450°C during 80 hours.

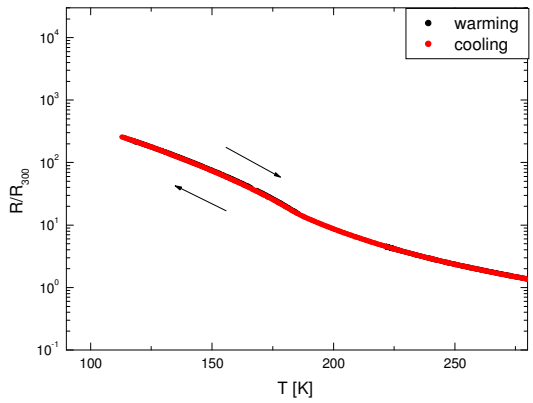

Fig. 4.1.1.3. *Temperature dependence of resistivity of V_2O_3 thin film annealed at 300 °C*

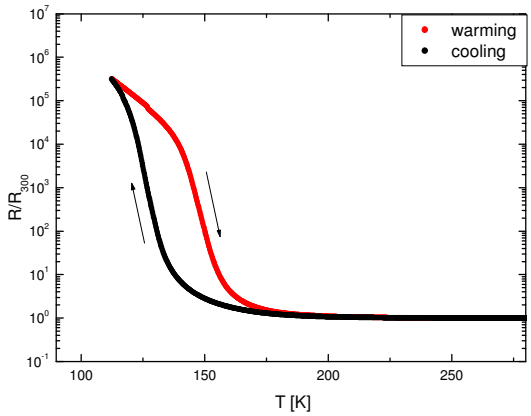

Fig. 4.1.1.4. *Temperature dependence of resistivity of V_2O_3 thin film annealed at 360 °C*

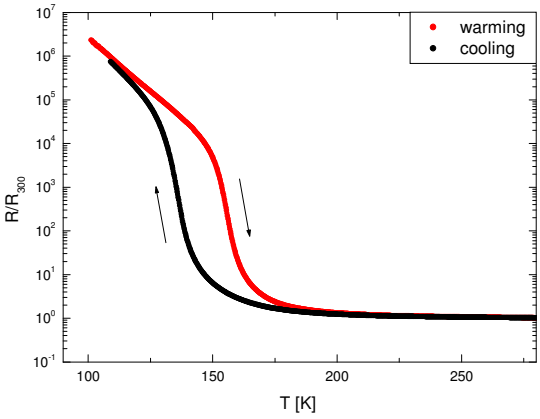

Fig. 4.1.1.5. *Temperature dependence of resistivity of V_2O_3 thin film annealed at 400 °C*

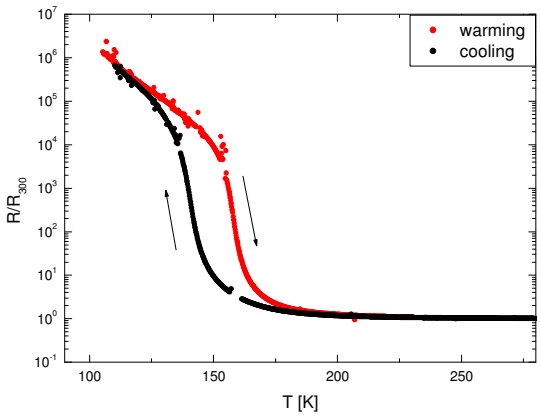

Fig. 4.1.1.6. *Temperature dependence of resistivity of V_2O_3 thin film annealed at 450 °C*

The V_2O_3 thin film annealed at 300°C does not show a pronounced metal to insulator transition (Fig. 4.1.1.3). On the other hand the samples annealed at higher temperatures (360 - 450°C) manifest clear a MIT (Fig. 4.1.1.4 - 4.1.1.6) which is accompanied by a large resistivity jump of about six orders of magnitude. However,

MITs of these thin films are broader than in bulk crystals and the transition temperatures are lower. Moreover, the temperature of MIT is strongly dependent on the annealing conditions.

To check the tendency of the variation of T_{MIT} with annealing in the present work a detailed study with smaller steps in annealing temperature was done. The results are presented in Fig. 4.1.1.7, which shows the temperature dependencies of the resistance for samples, annealed at temperatures 350 - 450°C.

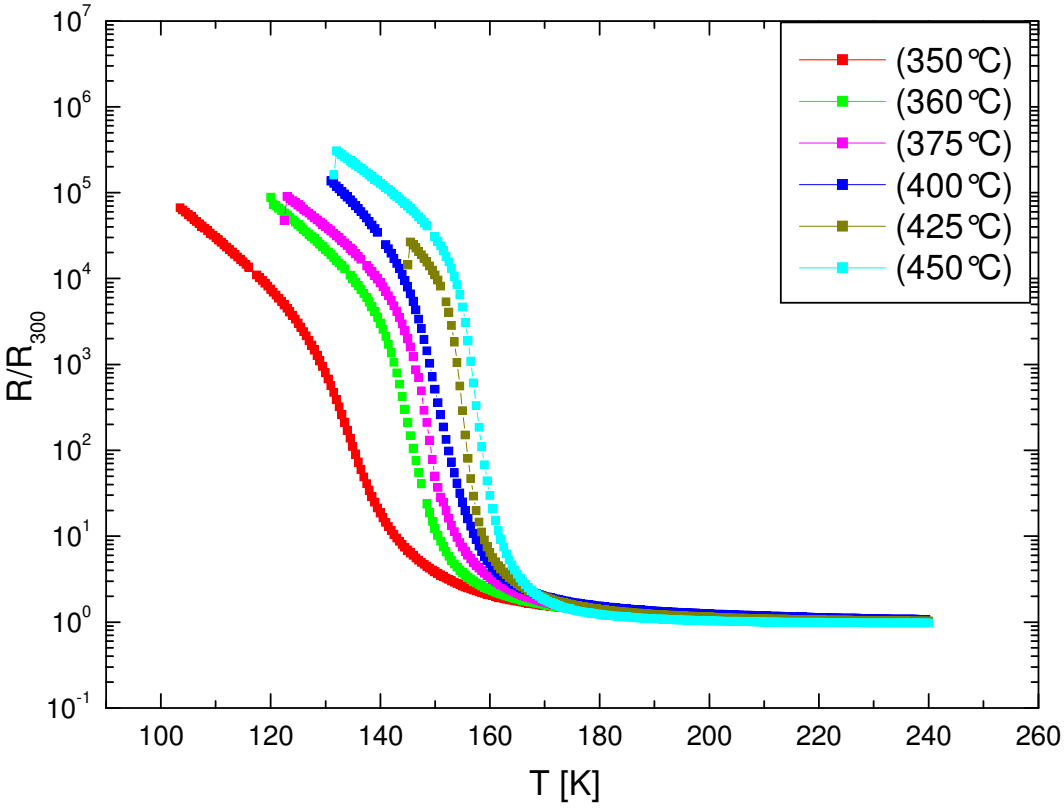

Fig. 4.1.1.7. *Temperature dependence of the resistance (cooling runs) for samples, annealed at different temperatures in the region 350 - 450 °C.*

As is clearly seen, the transition temperature (T_{MIT}) depends on the thermal treatment temperatures and T_{MIT} of the film annealed at lower (350°C) temperature (red line) is far below T_{MIT} of the thin films annealed at higher temperature (450°C)

(light blue line). Thus, an increase of the annealing temperature results in an increase of T_{MIT} as summarized in Fig. 4.1.1.8.

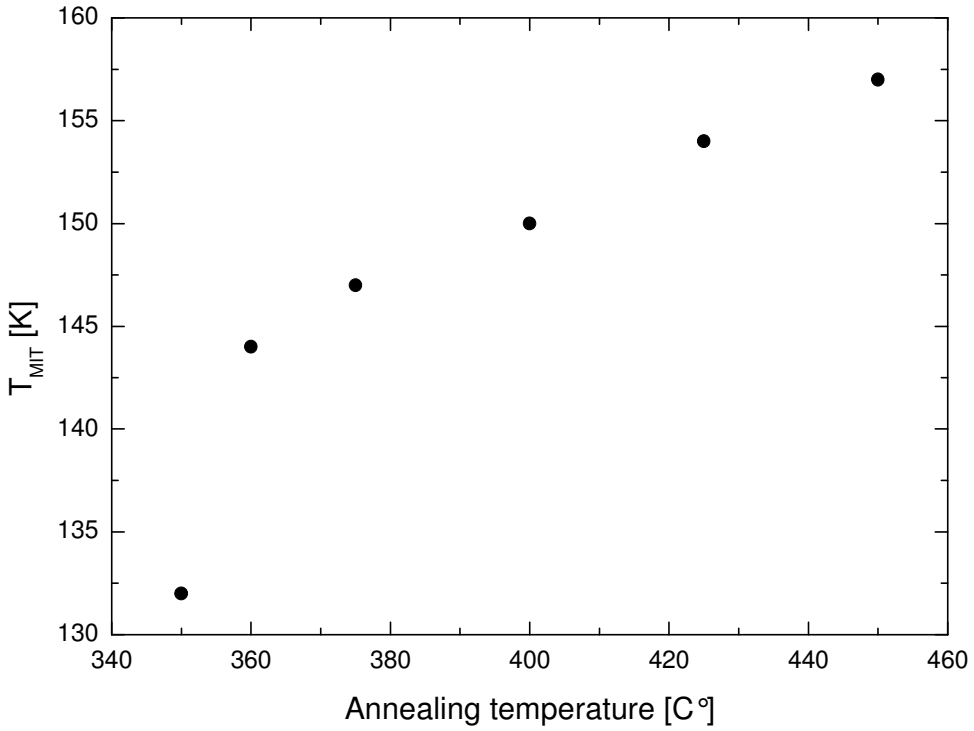

Fig. 4.1.1.8. *Dependence of T_{MIT} on the annealing temperature.*

In the range of annealing temperatures T_a = 350 - 360°C, a strong increase of the T_{MIT} occurs. For higher annealing temperatures the empirical dependence of the transition temperature as a function of annealing temperature becomes practically linear. The value of the T_{MIT} for the highest annealing temperature (450°C) approaches the T_{MIT} of the bulk material, T_{MIT}(bulk) = 165 K.

Another important result of the present work is related to the width of the metal to insulator transition (ΔT_{MIT}). The width, defined as was shown in Chapter 3.2.5, also shows strong correlation with annealing temperatures. The obtained data are presented in Fig. 4.1.1.9.

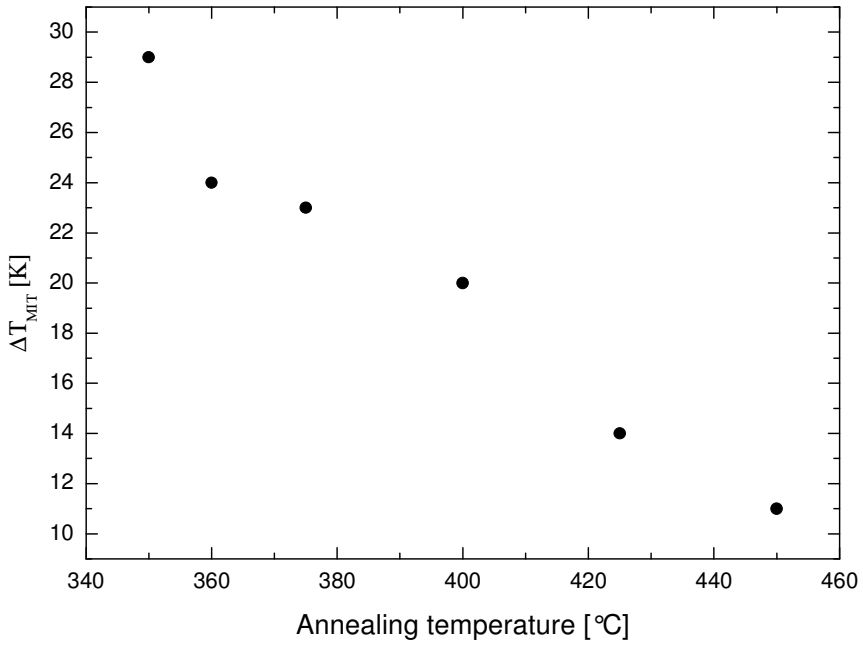

Fig. 4.1.1.9. *Dependence of width of T_{MIT} on annealing temperature.*

With decreasing annealing temperature a steep increase of the ΔT_{MIT} is observed for the samples annealed between 350 and 360°C, followed by a more smooth dependence in the temperature range 370 - 450°C. Table 4.1.1 summarizes the obtained results.

Annealing temperature, °C	300	350	360	375	400	425	450
T_{MIT}, K	No transition	132	144	147	150	154	157
(ΔT_{MIT}), K		29	24	23	20	14	11

Table 4.1.1. *Correlation between annealing and transition temperatures and width of MIT.*

The decrease of T_{MIT} for lower annealing temperatures can be caused by strain and the broadening of the transition width in resistivity experiments might be also related to increase of the strain. This effect is evidently connected with a smaller lattice constant of the film compared to that of the bulk material. The film is just subjected to stress, which has the similar effect as an externally applied pressure. It is well known that such a pressure also reduces the transition temperature (see Chapter 2.2.1). It is necessary to note additionally the effect of the oxygen nonstoichiometry, which can contribute to the decrease and broadening of the metal to insulator transition temperature. To study the above mentioned phenomena additional measurements were done (see the following chapters).

4.1.2 Atomic Force Microscopy (AFM)

The AFM pictures for three samples annealed at different temperatures are presented in Fig. 4.1.2.1 - 4.1.2.3.

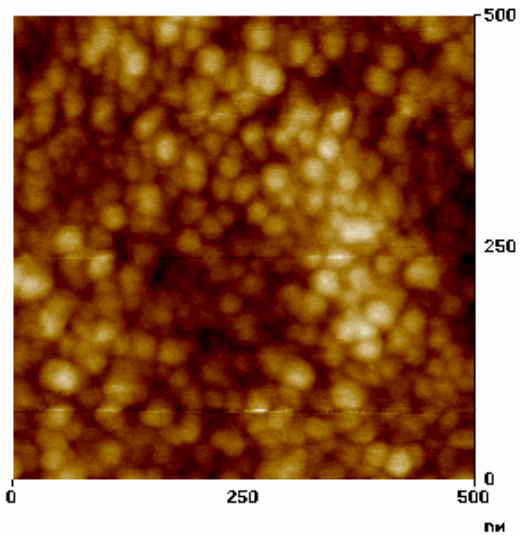

Fig. 4.1.2.1. *AFM image of a V_2O_3 thin film annealed at 360°C*

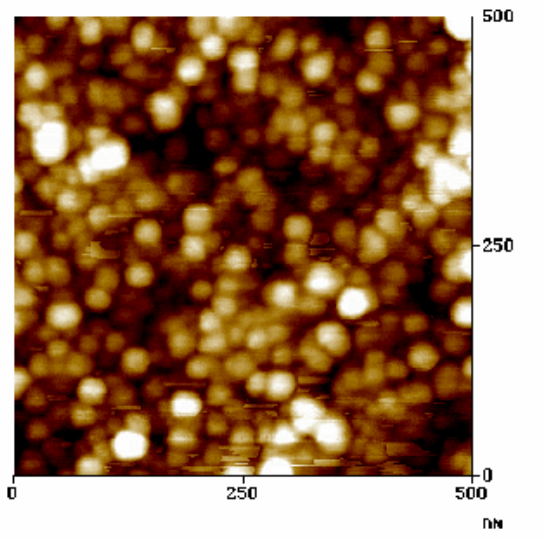

Fig. 4.1.2.2. *AFM image of a V_2O_3 thin film annealed at 400°C*

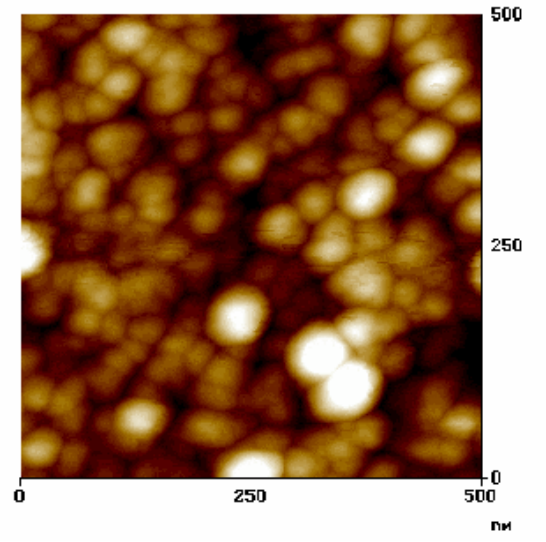

Fig. 4.1.2.3. *AFM image of a V_2O_3 thin film annealed at 450°C*

As clearly seen, the increase of annealing temperatures is accompanied by a notable increase of the grain size. E.g. the grain size for the sample annealed at 360°C is 20 - 25 nm and increases to 30 - 35 nm and 40 - 45 nm for the samples annealed at 400°C and 450°C, respectively. Therefore, the increase of the grain size probably explains the reduction of internal stress in the samples by increasing annealing temperatures, and agrees well with the above mentioned behavior of the T_{MIT} and ΔT_{MIT} as a function of annealing temperature. It has to be noted that the V_2O_3 thin films annealed at temperature higher than 450°C crack during annealing. An example of such cracks is shown by optical microscope image (Fig. 4.1.2.4).

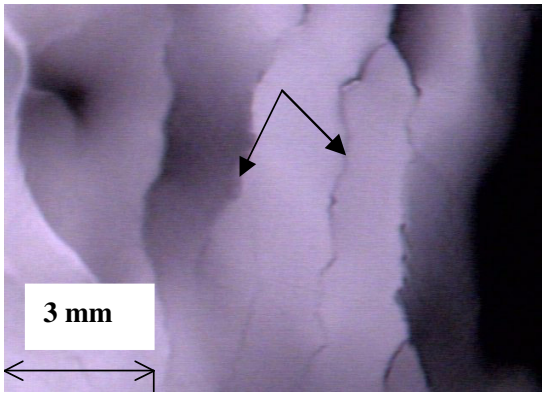

Fig. 4.1.2.4. *Optical image of cracked V_2O_3 film annealed at 480°C (arrows indicate cracks).*

4.1.3. Dynamic Secondary Ion Mass Spectrometry (SIMS)

To check the homogeneity of V_2O_3 thin films grown on the diamond substrate, dynamic secondary ion mass spectrometry (SIMS) measurements were carried out. In Fig. 4.1.3 the depth profile of V and O ions are presented.

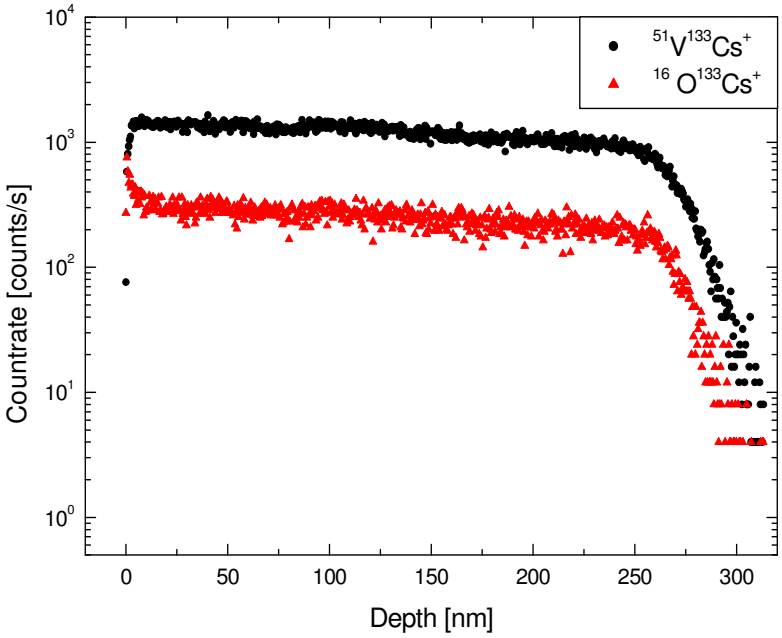

Fig. 4.1.3. *Depth profile of the intensity of V (black line) and O ions (red line).*

The measured profile demonstrates a rather good depth homogeneity of the V_2O_3 film with minor scattering of intensity within the limit of accuracy of the method. The initial (up to a depth of 5 nm) variation of V and O is probably related to surface effects. Additionally one can determine the thickness of the film, d ~ 270 nm. All films investigated in the present work show a similar behavior and, therefore, are not presented here. Because the SIMS measurements cannot give quantitative information on the stoichiometry, additional measurements like XRD and RBS were performed.

4.1.4 X-ray Diffraction (XRD) Measurements

X-ray diffraction pattern (θ/2θ or Guinier geometry) for samples annealed at three different temperatures (360 - 450°C) are shown in Fig. 4.1.4.1. The X-ray peaks related to V_2O_3 thin films are clearly visible at angles between 20° and 40°.

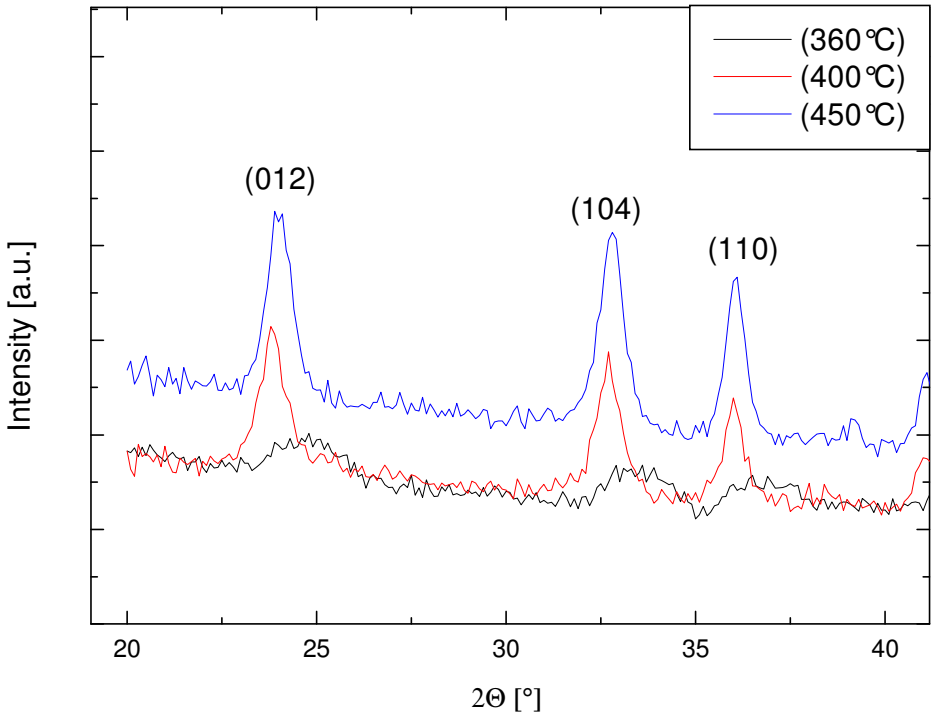

Fig. 4.1.4.1. *X-ray diffraction measurements of V_2O_3 thin films deposited on diamond substrate.*

The diffraction patterns for three samples show clear dependence on the annealing temperature. The most stochiometric sample (annealed at 450°C, blue line) shows the sharpest and narrowest peak, while peaks for the samples annealed at low temperatures (360 - 400°C, black and red lines) are broadened and even shifted to higher angles (360°C, black line). Thus, the obtained results indicate the presence of nonuniform distribution of the strain with decreasing annealing temperatures. The shift of the X-ray diffraction lines for the samples annealed at 360°C may be also caused by

some uniform distribution of the strain. These results are in general correlation with the theory (see Chapter 3.2.3).

The X-ray diffraction pattern of V_2O_3 thin film annealed at 400°C in a broad range of Θ/2Θ angles are presented in Fig. 4.1.4.2.

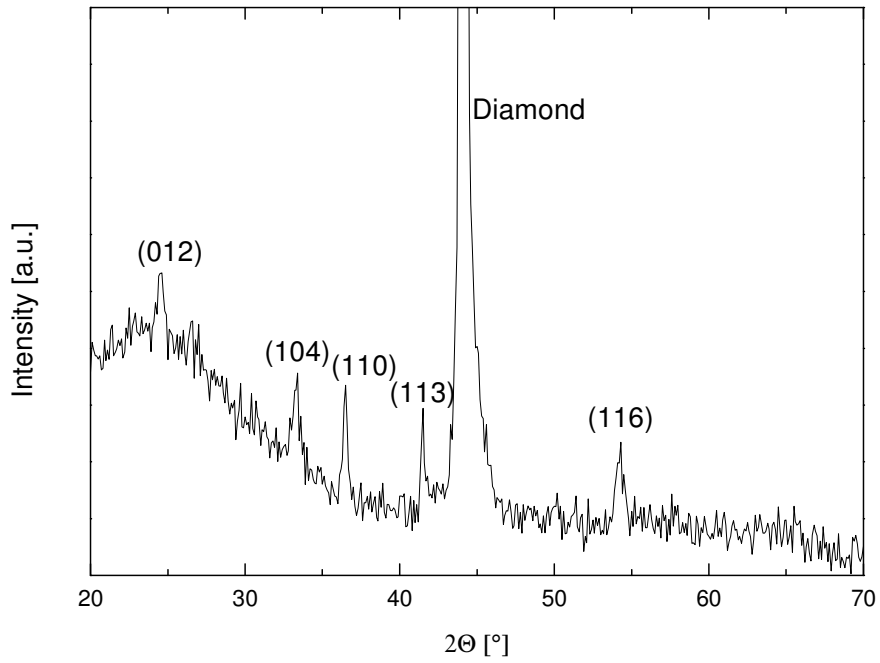

Fig. 4.1.4.2. *X-ray diffraction measurements of V_2O_3 thin film annealed at 400°C*

The peaks ((012), (104), (110), (113), (116)) related to V_2O_3 can be clearly seen, however all peaks are shifted to higher angles compared to bulk material. A careful analysis of the shifts of the diffraction peaks related to V_2O_3, can give information about the lattice parameter of V_2O_3 films. To get reasonable results for the lattice parameters, the used diffractometer has to be calibrated. Especially the shifted peaks because of the artificial vertical displacement of the thin film deposited on a thick diamond substrate have to be eliminated. Therefore, an individual reference measurement was done for every analyzed film. The vertical displacement was measured by covering the film with fine Si powder and fitting the well known peak pattern by adjusting the Si lattice constant and the vertical displacement parameter with Powder Cell [Kraus1999]. The deviation of the adjusted lattice parameter to that

known from the literature was less than 0.003 %. The remaining peak shifts (after having subtracted Cu-$K_{\alpha 2}$ line) concerning the V_2O_3 film have now to be fitted only with the adequate lattice parameters.

Several peaks for every film have been measured with acceptable precision with respect to intensity. With respect to the measurement time the measurements could only be done with increment steps of 0.1°. But with this apparently poor resolution it is possible to determine the maximum position of every peak with an accuracy between 0.02° and 0.05°, resulting in a relative error of the parameter *a* of better than 0.10% and a relative deviation of the parameter *c* better than 0.18%. Because of the poor step rate it was not possible to determine the peak form and the peak width. Taking into account all above mentioned peak positions for every film, it is possible to fit all the peaks for one film with the same unit cell parameters *a* and *c*. This means that independent on the orientation of the grains of a film all of them have the same strain. In that way the error for the *a* and *c* parameter decreases to 0.04% and 0.07% respectively. The fine powder (Si) could easily be removed without affecting the film.

The typical example for shifted reflection (110) is presented in Fig. 4.1.4.3. The vertical line (red) shows the peak position of the bulk material.

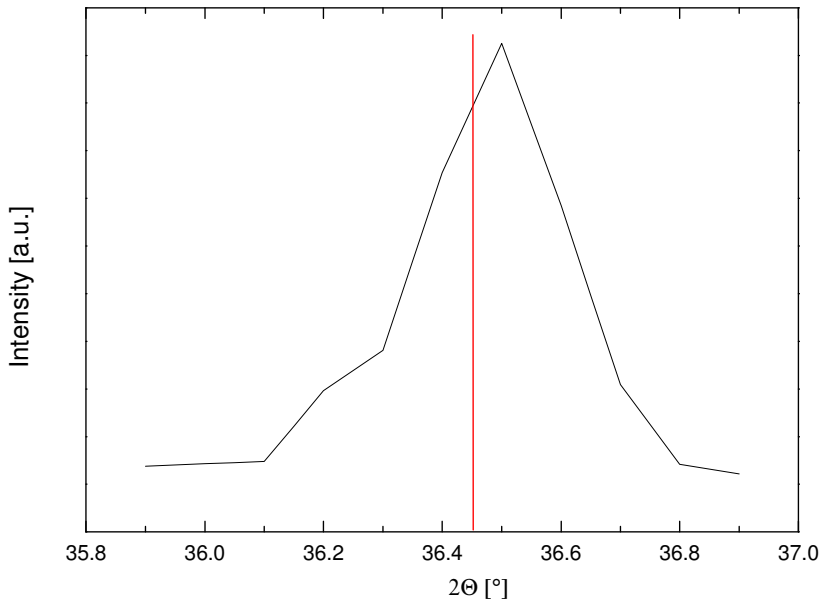

Fig. 4.1.4.3. *Diffraction peak of V_2O_3 thin film (100).*

Such calculations were done for the thin films annealed at three different temperatures (360, 400, 450°C) and the results of this study are summarized in table 4.1.4.

Annealing temperature, °C	360	400	450	Bulk material
Change of the lattice constant ***a***	-0.16%	-0.10%	-0.08%	-0.02
Change of the lattice constant ***c***	-0.31%	-0.31%	-0.31%	0
ΔV/V	-0.63%	-0.51%	-0.47	-
P, GPa	1.14	0.92	0.85	**-**
$T^{C}_{MIT,}$ K	117	129	134	**-**
T^{EX}_{MIT}, K	144	150	157	165

Table 4.1.4. *Change of the lattice constants (a, c) with annealing temperature.*
ΔV/V is volume change compare to bulk material
P is a pressure, necessary to yield the respective volume change
T^{C}_{MIT} – the calculated transition temperature accounting for the pressure change
T^{EX}_{MIT} – the experimental value of the transition temperature.

As is seen from these results all samples have a smaller lattice parameter *c* compared to the bulk material, which does not depend on the annealing temperatures. This reduction of the lattice constant can be probably explained as due to nonuniform strain, induced by the substrate during the thin film preparation. Appearance of such a nonuniform strain is well known for thin films of manganite [Biswas2000] and different semiconducting films [Chen1999]. Independence of the lattice constant *c* on the annealing temperatures indicates that this strain is rather strong and can not be released by the thermal treatment. However, the *a* parameter shows a continuous change with increasing annealing temperature, and approaches to that of the bulk material for the optimal annealing temperature (450°C).

Comparison of the experimental and calculated values of the T_{MIT} shows some overestimations of the pressure effect derived from the phase diagram. This probably may be related to the different type of the strain in the thin film and in the bulk material.

4.1.5 Rutherford Backscattering Spectrometry (RBS)

Fig. 4.1.5.1 - 4.1.5.3 shows RBS spectra (red lines) of thin films annealed at three (360 - 450°C) different temperatures. The resulting spectra were fitted (black lines) using the software [RUMP].

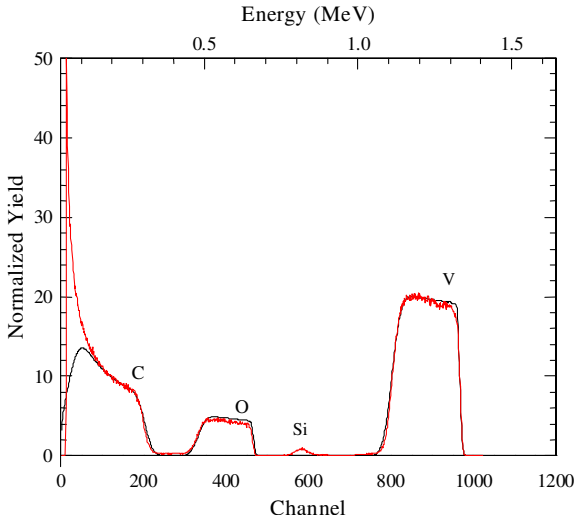

Fig. 4.1.5.1. *RBS spectra for sample annealed at 360°C.*

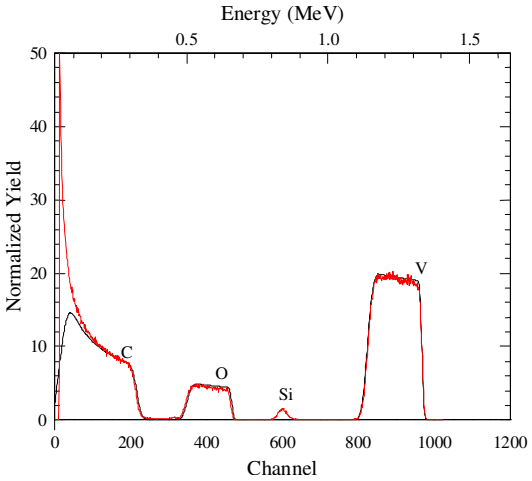

Fig. 4.1.5.2. *RBS spectra for sample annealed at 400°C.*

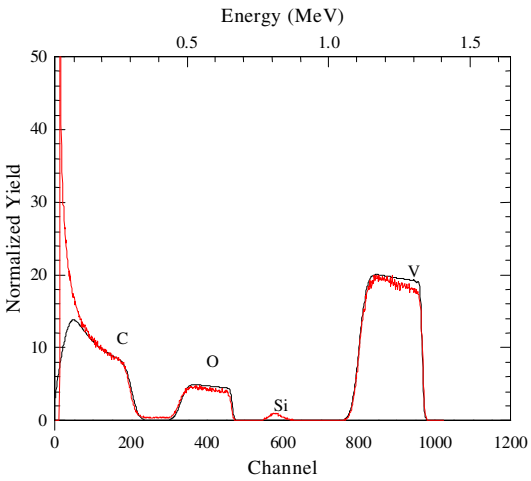

Fig. 4.1.5.3. *RBS spectra for sample annealed at 450°C.*

The RBS spectra analysis revealed that O/V - ratio varies between the samples and this variation depends on the annealing temperature. The fact that diamond was grown on Si substrate can explain the observed presence of Si between the diamond and V_2O_3 thin film. In the Table 4.1.5 the relations between O/V – ratio and annealing temperature are presented.

Annealing temperature, °C	360°	400°C	450°C
O/V	1.84±	1.82±	1.81±0.05

Table 4.1.5. *Relations between the O/V - ratio and annealing temperature.*

Thus, RBS spectra for samples annealed at lower temperature (360°C) show a deviation from the stoichoimetric V_2O_3, and the increase of the annealing temperature leads to a decrease of the O/V ratio, which shows a tendency to approach the stoichiometric value at higher annealing temperatures. The enhanced ratio of O to V obtained from the RBS measurements might be related to the presence to some extent of the vanadium oxides with higher oxidation states (like VO_2, V_2O_5). However, the XRD does not show such binary oxides within experimental error ~2 % and this question still remains unclear. One of the explanations might be that the V_2O_3 grains are coated by V_2O_5 and in this case calculations for 20 nm of V_2O_3 grain size (see Chapter 4.1.2) give the value of thickness of V_2O_5 coating of about ~ 0.7 nm. Such a relatively small amount can not be detected by XRD measurements.

4.1.6 Conclusion

The resistivity measurements of the V_2O_3 thin films grown by developed method show a strong dependence of the metal to insulator transition temperature on the annealing temperature. Namely, the phase transition temperature (T_{MIT}) increases and the width of the transition decreases with increasing annealing temperature. Concomitantly, the size of the crystallites increases from 20 to 50 nm with increasing of annealing temperature from 360 to 450°C, respectively.

X-ray measurements show a strong decrease of the lattice volume of films compared to the bulk material. At the same time the difference between thin films and bulk material is reduced with increasing annealing temperature and the lattice constant *a* is approaching the value for bulk material. All these results are in good agreement and can be explained within the strain induced by diamond substrate.

The RBS measurements show a deviation of the chemical composition from the stoichiometry, suggesting the presence of vanadium oxides in higher oxidation state. The RBS data however exhibit continuos approach to the stoichiometry with increasing annealing temperature. These results are in good correlation with the resistivity and X-ray data.

4.2 V_2O_3 Thin Films Grown on $LiNbO_3$ Substrates

The possibility of direct deposition of V_2O_3 films on a $LiNbO_3$ substrate allows to investigate the temperature dependent electrical, dielectric and elastic properties of V_2O_3 at the metal to insulator transition by measurements of the propagation of surface acoustic waves (SAW). In this Chapter the structure of V_2O_3 films on $LiNbO_3$ as well as results on the attenuation and sound velocity of SAW in the temperature range from 260 K to 10 K are presented.

4.2.1 X-ray Diffraction (XRD) Measurements

The structure of V_2O_3 thin films, grown on $LiNbO_3$ substrates, was characterized by X-ray diffraction (XRD) measurements, carried out in the Θ–2Θ mode for 2Θ = 35°- 65°. The corresponding XRD pattern is shown on Fig. 4.2.1.

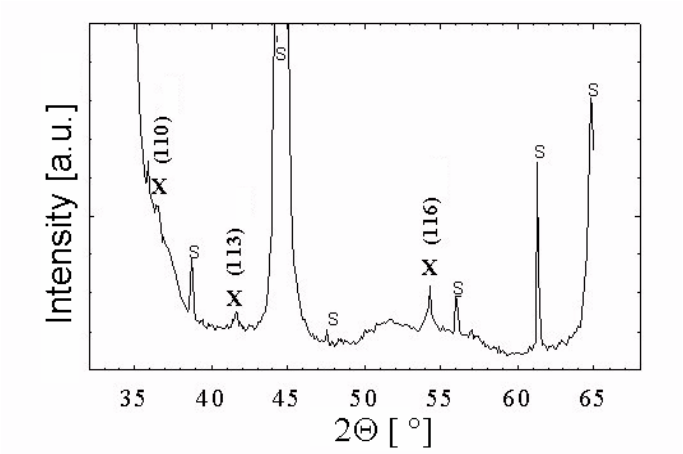

Fig 4.2.1. *XRD measurements of a V_2O_3 thin film deposited on $LiNbO_3$. X: V_2O_3 peaks; S: Substrate and sample holder peaks.*

In Fig. 4.2.1 the Bragg peaks (110), (113), (116) of V_2O_3 can be clearly seen. The fact that no other V_2O_3 peaks are observed indicates a partially textured structure of the film. The other diffraction peaks seen in Fig. 4.2.1 originate from the $LiNbO_3$ substrate, the metallic IDTs and the aluminium sample holder. From the peak positions a reduction of the *c* - parameter by ~ 0.5% compared to bulk V_2O_3 is estimated. Within experimental accuracy the *a* **-** axis lattice constant is the same as that of the bulk material. For this analysis the shift (~ 0.2°) of the peaks due the thickness of the sample was taken into account.

4.2.2 Atomic Force Microscopy (AFM)

In Fig. 4.2.2 we show a characteristic AFM image of the V_2O_3 thin film deposited on $LiNbO_3$ substrate, taken in the tapping mode.

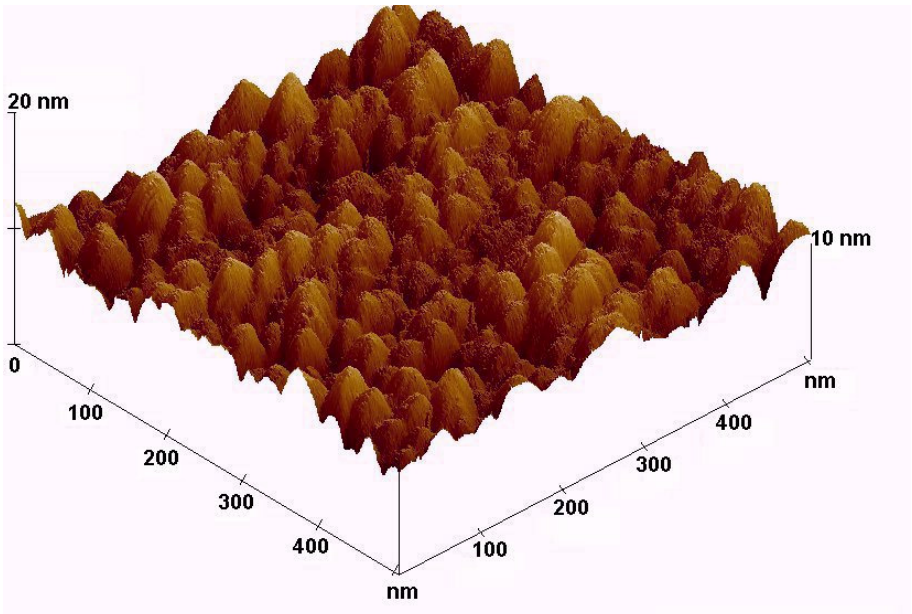

Fig. 4.2.2. *Three dimensional AFM image of a V_2O_3 thin film deposited on a $LiNbO_3$ substrate.*

The microstructure of the film is characterized by the presence of crystalline grains with average grain size varying as 15 - 25 nm.

4.2.3 Resistivity Measurements

The resistivity of a V_2O_3 thin film grown on a $LiNbO_3$ substrate was measured by the four point method (see Chapter 3.2.4). Fig. 4.2.3 shows the results of the DC resistivity and the sheet conductance measurements.

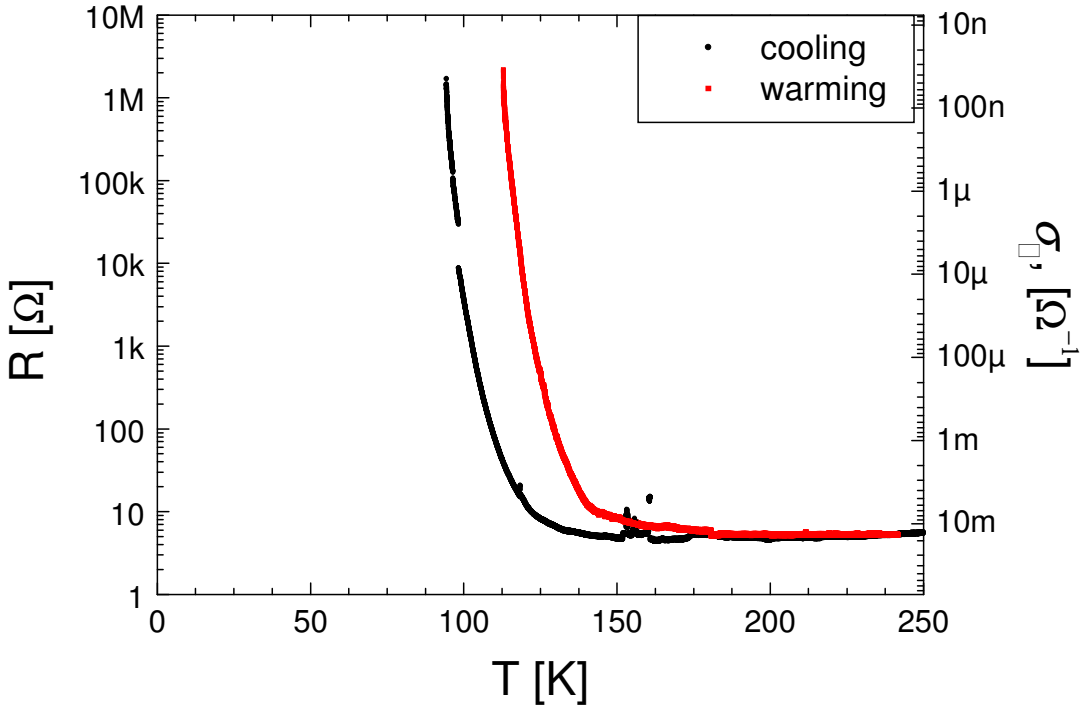

Fig. 4.2.3. *Temperature dependence of the resistance and sheet conductance $\sigma_{\square}$, respectively of V_2O_3 thin film deposited on a $LiNbO_3$ substrate.*

The resistivity at the metal to insulator transition (MIT) at 95 K (cooling run) jumps by about six orders of magnitude. A hysteresis between the resistivity values for cooling (black line) and warming (red line) of about 17 K was observed. However, the temperature of the MIT is low and the value of hysteresis between cooling and warming is about two times larger than that seen in stoichiometric bulk material. These effects can be explained by the reduced *c* - axis lattice parameter (see Chapter 4.2.1).

From the measured resistivity of the V_2O_3 thin film the sheet conductance was obtained by

$$\sigma_{\square} = R_{\square}^{-1} = d/\rho,$$

where the resistivity of the film is

$$\rho = R \cdot (w \cdot d)/L,$$

with w the width of the film, L the distance of the voltage probes and d the thickness of the thin film (L = 200 µm, w = 2.7 mm, and d = 370 nm).

4.2.4 Surface Acoustic Waves (SAW) Investigations

Attenuation

The temperature dependence of the attenuation signal of the surface acoustic wave is presented in Fig. 4.2.4.1. In the metallic phase the mobility of electrons is very high so they can rearrange with electrical field of the SAW; in the insulating phase the mobility is very low and the electrical field of the SAW can not influence the electrons. In both cases the attenuation is small and nearly constant (see Fig. 2.4.3(a)). The attenuation is maximal at a temperature close to the MIT mainly caused by the change of the conductance between metallic and insulating states of the V_2O_3 thin film.

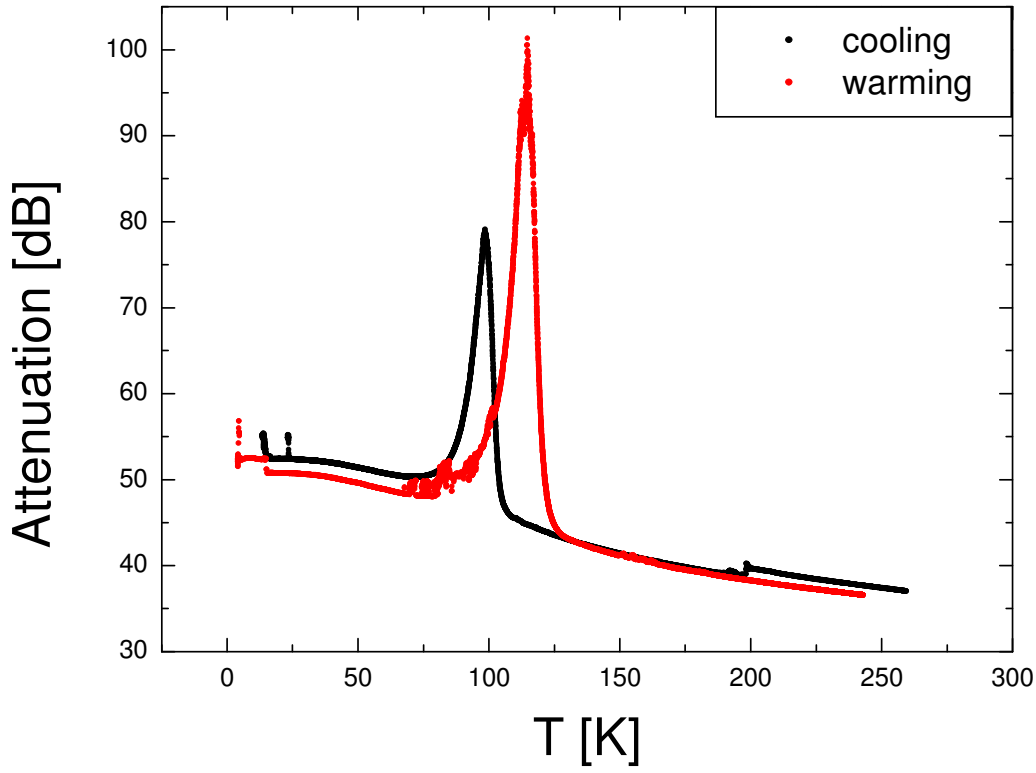

Fig. 4.2.4.1. *Temperature dependence of the surface acoustic wave attenuation.*

The measured attenuation signal shows a hysteresis between cooling (black line) and warming (red line). The hysteresis has the same width compared to the hysteresis observed by resistivity measurements (see Chapter 4.2.3). Thus, the maximum of the SAW attenuation on cooling ~ 75 dB appears at 95 K, and on warming ~ 95 dB at 115 K respectively. The observed noise below 20 K may be explained by the adsorption of helium on the V_2O_3 thin film, resulting in an additional damping of the SAW. The results after a removal of the baseline which increases with decreasing temperature are plotted in Fig. 4.2.4.2(a)

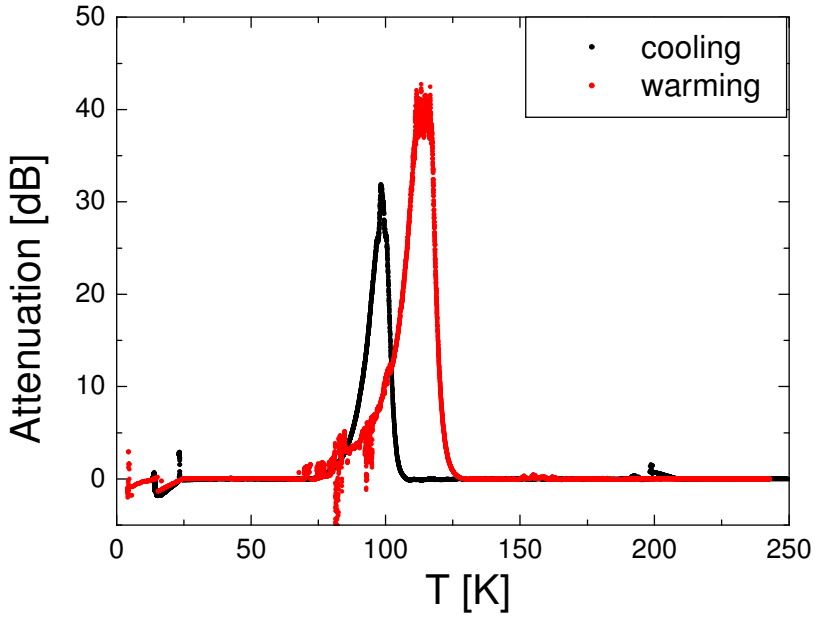

Fig. 4.2.4.2(a). *Measured temperature dependence of the attenuation of a surface acoustic wave.*

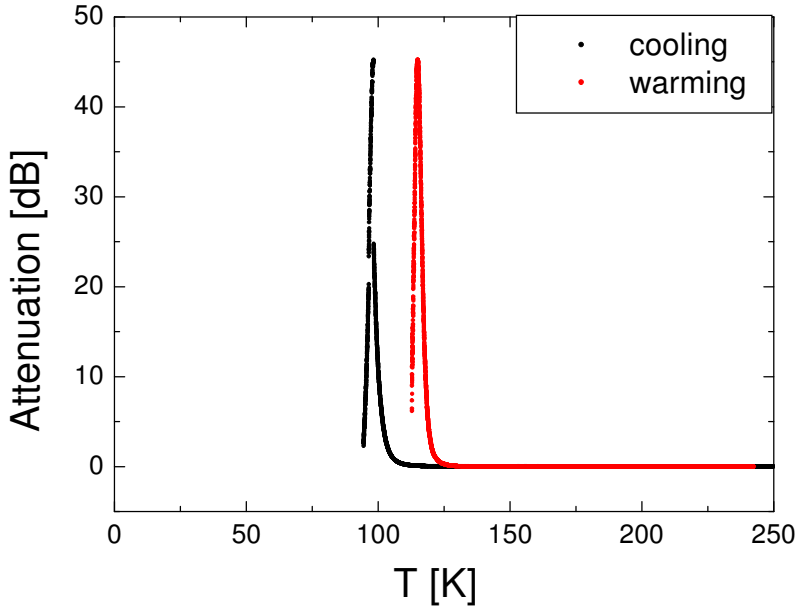

Fig. 4.2.4.2(b). *Calculated temperature dependence of attenuation of a surface acoustic wave.*

Using the measured values for the DC sheet conductance (see Chapter 4.2.3) and Eq. 2.3.2 (see Chapter 2.3) the absorption coefficient Γ has been calculated. For a quantitative comparison of measured and calculated Γ – coefficient, it was considered that the electrical signal of the SAW decreases between sending and receiving IDTs by a factor of $F = \exp(-\Gamma L_F)$. The attenuation in dB units is $10 \log F^2$. Results of the calculations for the attenuation are shown in Fig. 4.2.4.2(b).

The maxima of the measured and calculated temperature dependence of the attenuation appear at the same temperature (95 K on cooling and 115 K warming). The DC resistance was not measured to very low temperatures and this limits the temperature range covered by the calculation The difference in σ_m (see Chapter 2.3) values ($\sigma_m = 2.5*10^{-6}\ \Omega^{-1}$ (cooling) and $\sigma_m = 0.5*10^{-6}\ \Omega^{-1}$ (warming)) may be explained by a changing of the relative permittivity of the V_2O_3 thin film or by a percolation of the current in the DC conductivity measurement with different paths for cooling and warming. The value for the pure substrate is $\sigma_m = 2*10^{-6}\ \Omega^{-1}$ [Datta1986].

Sound velocity

The change of the sheet conductance of the coating thin film results in a change of the sound velocity. This is mainly due to the fact that a metal like film short-circuits the electrical restoring forces, whereas an insulating one does not.

Fig. 4.2.4.3 shows the measured sound velocity shift of a V_2O_3 thin film (black line) and the calculated sound velocity shift (blue line) defined by Eq. 2.3.2 (see Chapter 2.3).

The data of the measured curve (black line) start to deviate from the theoretical one (blue line) at around 200 K. This deviation can be fitted by a polynomial of second order (red line).

In the temperature range 200 - 110 K this polynomial was subtracted and the result of this subtraction is presented in Fig. 4.2.4.4.

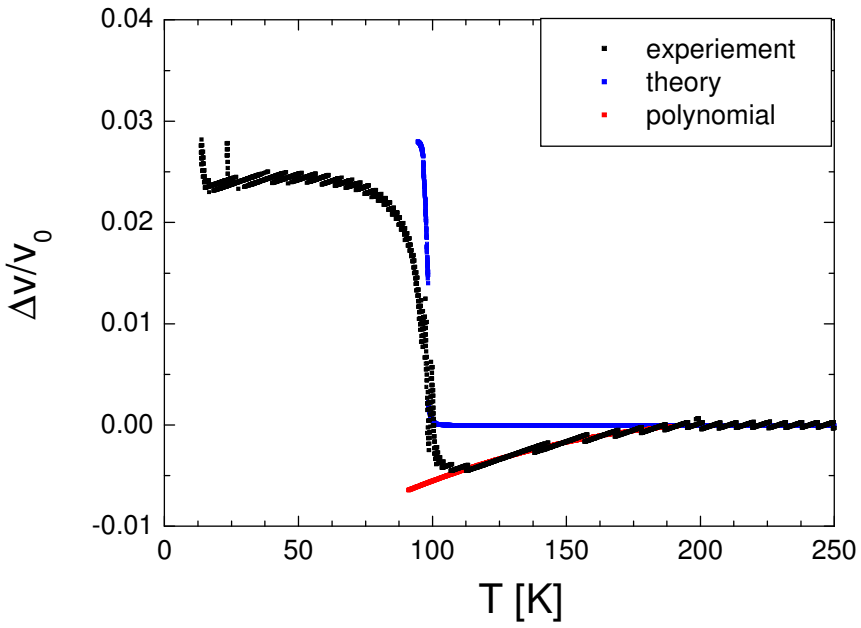

Fig. 4.2.4.3. *Temperature dependence of the sound velocity shift of a surface acoustic wave (cooling run).*

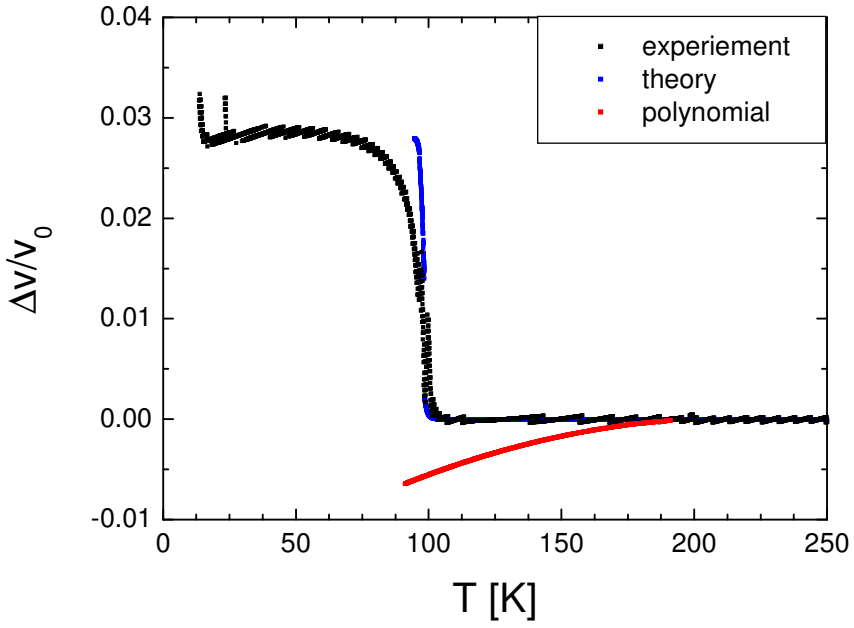

Fig. 4.2.4.4. *Temperature dependence of the sound velocity shift of a surface acoustic wave (cooling run).*

The step height of measured and calculated curves are equal, and describe the difference of the velocities of $LiNbO_3$ covered by an insulating and a conducting thin film expressed by Eq. 2.3 (see Chapter 2.3). There is a smoother increase of the measured sound velocity at lower temperatures compared to the theoretical one. The same behavior was seen for the attenuation (the attenuation peaks are broader compared to theory) (see Fig. 4.2.4.2 (a)(b)).

4.2.5 Conclusion

V_2O_3 thin films directly deposited onto a piezoelectric $LiNbO_3$ substrate by using the technological method developed in the present work maintain their properties. This gives the possibility to investigate the attenuation and the sound velocity shift of a surface acoustic wave interacting with the V_2O_3 thin film. The thin films were characterised by X-ray diffraction and atomic force microscopy. From XRD measurements diffraction peaks related to V_2O_3 were observed. Other additional patterns are related to the substrate or the sample holder. The typical grain size of thin films observed by AFM was of about 15 - 20 nm. The resistivity jump of V_2O_3 grown on a $LiNbO_3$ substrate has about six orders of magnitude at the MIT, which is comparable to the bulk material. Using measured values for the DC sheet conductance the adsorption coefficient was calculated. The calculated temperatures of the maxima of the attenuation ($\sigma_m = 2.5*10^{-6}\ \Omega^{-1}$ (cooling) and $\sigma_m = 0.5*10^{-6}\ \Omega^{-1}$ (warming) are in a good agreement with the measured ones. The softening in the sound velocity shift which is observed above the resistivity jump could be possibly understood by an interplay between the orbital and lattice degrees of freedom and might be considered as a precursor of the MIT phase transition. In this context it should be noted, that the EXAFS measurements made by Pfalzer *et al*. [Pfalzer2006] show also a structural precursor for V_2O_3 single crystals above the MIT.

Summary

In the present work the following main scientific results were obtained:

- A new technology for the growth of V_2O_3 thin films was developed. The idea of this method is to grow thin films in two stages: 1 – deposition on cool substrates (T_{sub} = 300 K); 2 – subsequent annealing under controllable conditions. Such growth strategy allows to obtain stable V_2O_3 thin films on different substrates (diamond and $LiNbO_3$) at a reduced temperature compared to conventional UHV techniques.

- A detailed study of the structural properties of V_2O_3 thin films by means of atomic force microscopy, dynamic secondary ion mass spectrometry (SIMS) X-ray diffraction and Rutherford backscattering spectrometry was performed. The results of these measurements exhibit that V_2O_3 thin films grown by the new method have good structural properties. Thus, V_2O_3 thin films are homogeneous (the V/O ration is constant in the thin film volume), and have partially textured structure. The observed grain sizes are between 20 - 45 nm and depend on the annealing temperature.

- Electrical properties, particularly at the MIT, were studied by resistivity measurements. The electrical and structural studies are in good mutual agreement. The MIT of V_2O_3 was also investigated by SAW using the first directly deposited V_2O_3 thin film onto a $LiNbO_3$ substrate. A softening of the sound velocity shift, which occurs at about 60 K above the resistivity jump in the paramagnetic metallic phase, provides experimental evidence for a precursor of the MIT of V_2O_3.

- The thin films obtained in this work have the following parameters: a resistivity jump of six orders of magnitude and a T_{MIT} in the range 132 - 157 K; a width of transition of 11 - 29 K. The elaborated technology allows to vary and to adjust the T_{MIT} of V_2O_3 thin films by thermal treatment in a wide temperature range.

- V_2O_3 thin films grown on diamond substrates show a large resistivity jump at the metal to insulator transition (MIT), comparable to that observed in bulk material. The pronounced MIT behavior of V_2O_3 thin films on diamond substrates offers promising opportunities for application in various optical technologies. The V_2O_3 thin films might be useful, for example, for designing optical filters and infrared mirrors, which are of great interest for modern engineering.

- V_2O_3 thin films, directly deposited on a $LiNbO_3$ substrate by means of the developed technique, provide an interesting tool to study the peculiarities of the MIT by the propagation of surface acoustic waves (SAW).

Bibliography

[Biswas2000] A. Biswas, M. Rajeswari, R. C. Srivastava, Y. H. Li, T. Venkatesan, R.L. Greene. Two-phase behavior in strained thin films of hole-doped manganites. *Phys. Rev. B* **61** (2000).

[Born1927] M. Born, R. Oppenheimer. *Quantentheorie der molekel. Ann. Phys. (Leipzig)* **84**, 457 (1927).

[Castellani1978a] C. Castellani, C.R. Natoli, J. Ranninger. Insulating phase of V_2O_3: An attempt at a realistic calculation. *Phys. Rev. B* **18** (1978).

[Castellani1978b] C. Castellani, C.R. Natoli, J. Ranninger. Magnetic structure of V_2O_3 in the insulating phase. *Phys. Rev. B* **18** (1978).

[Chen1999] Y. Chen, J. Washbum. *Phys Rev Lett*. **77** (1999).

[Cox1992] P.A. Cox. Transition Metal Oxides: an Introduction to their Electronic Structure and Properties. *Charendon Press, Oxford* (1992).

[Datta1986] S. Datta. Surface acoustic Wave Devices. *Prentice-Hall, Englewood Cliffs, N.J.* (1986).

[Dernier1970a] P.D. Dernier. The Crystal Structure of V_2O_3 and $(V_{0.962}Cr_{0.038})_2O_3$ near the metal-insulator transition. *J. Phys. Chem. Solids* **31** (1970).

[Dernier1970b] P.D. Dernier, M. Marezio. Crystal Structure of the Low-Temperature Antiferromagnetic Phase of V_2O_3. *Phys. Rev B* **2** (1970).

[Feinleib1967] J. Feinleib, W. Paul. Semiconductor To Metal Transition in V_2O_3. *Phys. Rev.* **155** (1967).

[Elfimov2003] I.S. Elfimov, T Saha-Dasgupta, M.A. Korotin. Role of c-axis pairs in V_2O_3 from the band-structure point of view. *Phys. Rev. B* **68** (2003).

[Ezhov1999] S.Yu. Ezhov, V.I. Anisimov, D.I. Khomskii, G.A. Sawatzky. Orbital Occupation, Local Spin, and Exchange Interactions in V_2O_3. *Phys. Rev. Lett*. **83** (1999).

[Fazekas1999] P. Fazekas. Lecture notes on electron correlation and magnetism. *World Scientific* (1999).

[Foex1946] M. Foex. Etude dilatomemetrique et electrique de l'anomalie, presentee a basse temperature, par le sesquioxide de vanadium. *C. R. Acad. Sci.* 223 (1946).

[Frank1949] F.C. Frank, J.H. van der Merwe. *Proc. Roy. Soc. London*. A198, 216 (1949).

[Fabrizio1998] M. Fabrizio, M. Altarelli, M. Benfatto. *Phys. Rev Lett.* **80** (1998).

[Fock1930] V. Fock. *Z. Phys.* **61**, 126 (1930).

[Frenkel1997] A.I. Frenkel, E.A. Stern and F.A Chudnovsky. *Solid state Comm.* **102**, 637 (1997).

[Godwod1974] K. Godwod, R. Kowalczyk, Z. Szmid. Application of a Precise Double X-ray Spectrometer for Accurate Lattice Parameter Determination. *Phys. Sta. Sol.* **21** (1974).

[Goodenough1971] J.B. Goodenough. Metallic oxides. *Progress in Solid State Chem.* **5** (1971).

[Gutzwiller1963] M.C.Gutzwiller. Effect of correlation on the ferromagnetism of transition metals. *Phys. Rev. Lett.* **10**, 159 (1963).

[Hartree1958] D.R. Hartree. *Proc. Cambridge Philos. Soc.* **24**, 89. (1928).

[Hörner2005] A.L. Hörner. Untersuchingen von Metal-Isolator-Übergängen mit Oberflächenwellen. *PhD Thesis* Augsburg (2005).

[Hubbard1963] J. Hubbard. Electron correlations in narrow electron bands. *Proc. Roy. Soc.London.* **A 276**, 238 (1963).

[Imada1998] M. Imada, A. Fujimori, Y. Tokura. Metal-insulator transitions. *Rev. Mod. Phys*. **70**, (1998).

[Ingebrigtsen1970] K.A .Ingebrigsten. *J. Appl. Phys.* **41**, 454 (1970).

[Jayaraman1970] A. Jayaraman, D.B. McWhan, J.P. Remeika. Critical Behavior of the Mott Transition in Cr-Doped V_2O_3. *Phys. Rev. B*. **2** (1970).

[Jenkins1996] R. Jenkins, R.L. Snyder. Introduction to X-ray Powder Diffractometry. *Chemical Analysis: A Series of Monographs on Analytical Chemistry and Its Applications,* 138 (1996).

[Jones1989] R.O. Jones and O. Gunnarsson. The density functional formalism, its applications and prospects. *Rev. Mod. Phys*. **61**, 689. (1989).

[Kanamori1963] J. Kanamori. Electron correlation and ferromagnetism of transition metals. *Prog. Theor. Phys.* **30**, 275 (1963).

[Klimm1997] S. Klimm. Magnetotransportmessungen zur Untersuchung der elektronischen Struktur von V_2O_3 und MoO_2. *PhD Thesis* Augsburg (1997).

[Kotliar2004] G. Kotliar, D. Vollhardt. Strongly correlated materials: insights from dynamical mean-field theory. *Physics today* (2004).

[Kovacs1990] G. Kovacs, M. Anhorn, H.E.Engan, G.Visintini, C.C.W. Ruppel. Proc.-IEEEE Ultrason. Symp. (1990).

[Kraus1999] W. Kraus and G. Nolze. „PowderCell for Windows Version 2.3“. Computerprogramm. Bundesanstalt für Materialforschung und – prüfung (1999).

[Kuroda1977] N. Kuroda, H.Y. Fan. Raman scattering and phase transitions of V_2O_3. *Phys. Rev. B* **16** (1977).

[Landolt-Börnstein1981] Landolt-Börnstein Ferroelektrika und verwandte Substanzen. *Springer-Verlag, Berlin- -Heidelberg-New York.* **16** (1981).

[Mason1970] W. P. Mason, R.N. Thurston. Physical Acoustics. *Academic Press,* VI (1970).

[Matthews1977] H. Matthews Surface Wave Filters. *John Wiley&Sons,NewYork-London-Sydney-Toronto* (1977).

[McWahn70] D.B.McWhan, J.P.Remeika. Metal-Insulator Transition in $(V_{1-x}Cr)_2O_3$. *Phys. Rev. B* **2** (1970).

[McWahn71] D.B. McWhan, J.P. Remeika, T.M. Rice, W.F. Brinkman, J.P. Maita, A. Menth. Electronic Specific Heat of Metallic Ti-Doped V_2O_3. *Phys. Rev. Lett*. **27** (1971).

[McWahn71a] D.B. McWhan, A. Menth, J.P. Remeika. *J.Phys.Colloq* 1-3 (1971).

[McWhan73] D.B. McWhan, A. Menth, J. Premeika, W.F. Brinkman, T.M. Rice. Metal-Insulator Transitions in Pure and Doped V_2O_3. *Phys. Rev. B* **7** (1973).

[Mila2002] F. Mila, R. Shiina, F.-C. Zhang, A.Ma.M Joshi, V. Anisimov, T.M. Rice. Orbitally degenerate spin-1 model for insulating V_2O_3. *Phys. Rev. Lett*. **85** (2002).

[Morin1959] J.F. Morin. *Phys. Rev. Letters* **3** (1959).

[Mott1968] N.F. Mott. Metal-Insulator Transition. *Rev. Mod. Phys.* **40** (1968).

[Müller2005] C. Müller, A. A. Nateprov, G. Obermeier, M. Klemm, R. Tidecks, A. Wixforth, and S. Horn. Surface acoustic wave investigations of the metal-to-insulator transition of V_2O_3 thin films on lithium niobate. *J. Appl. Phys*. **98** (2005).

[Paolasini1999] L. Paolasini, C. Vettier, F. De Bergevin, F. Yakhou, D. Mannix, A. Stunault, W. Nuebeck, M. Altarelli, M. Farrizio, P.A. Metcalf, J.M Honig. *Phys Rev Lett,* **82** (1999).

[Park2000] J.-H. Park, L.H. Tjeng, A. Tanak, J.W. Allen, C.T. Chen, P. Metcalf, J.M. Honig, F.M.F. de Groot, G.A Sawatzky. Spin and orbital occupation and phase transitions in V_2O_3. *Phys. Rev B* **61** (2000).

[Pfalzer2004] P. Pfalzer. Lokale strukturelle und elektronische Eigenschaften von V_2O_3 und ZnV_2O_4. *PhD Thesis* Augsburg (2004).

[Pfalzer2006] P.Pfalzer, G. Obermeier, M. Klemm, S. Horn, M. L. denBoer. Structural precursor to the metal-insulator transition in V_2O_3. *Phys. Rev B* **73** (2006).

[Ratsch2003] C. Ratsch, J.A. Venables. Nucleation theory and the early stages of thin film growth. *J. Vac. Sci. Technol*, **A 21**(5) (2003).

[Shculer1997] H. Schuler, S. Klimm, G. Weissmann, C. Renner, S. Horn. Influence of strain on the electronic properties of epitaxial V_2O_3 thin films. *Thin Solid Films* **299** (1997).

[von Barth1972] U. von Barth and L. Hedin. A local exchange-correlation potential for the spin polirized case. *J. Phys, **C** **5**, 1629 (1972).

[Wixforth1989] A. Wixforth, J. Scriba, M. Wassermeier, J.P. Kotthaus. Surface acoustic waves on GaAs/$Al_xGa_{1-x}As$ heterostructures. *Phys. Rev. B* **40** (1989).

[Wixforth2000] A. Wixforth. Interaction of surface acoustic waves, electrons, and light. *International Jornal of High Speed Electronics and Systems* **10**, N4 (2000).

Acknowledgements

I specially thank Prof. Dr. Siegfried Horn for the possibility to work in his group on very interesting topic. He always gave a new ideas and impulses for my research.

I am grateful to Priv.-Doz. Dr. Helmut Karl for RBS and SIMS measurements and for fruitful discussion about results.

Thanks are due to Prof. Dr. Reichard Tidecks, Dr. Claus Müller and Dr. Andreas Hörner for very constructive discussion about SAW study.

I further want to thank Dr. Gunter Obermeier, Dr. Matthias Klemm, and Dr. Robert Horny for the help with resistivity and XRD measurements and who had always time to answer my questions.

I thank Dr. Vladimir Tsurkan and Dr. Vasily Moshnyaga for helpful discussion and valuable comments.

I also want to thank M. Krispin for qualitative AFM measurements, Dr. Ivan Leonov and Mikhail Sekania for theoretical support.

My sincere thanks are due to all members of the group of Prof. Dr. Horn for very friendly and creative atmosphere and every day support.

Finally, I want to thank my parents who always believe in me.

CURRICULUM VITAE

Name	Nateprov Alexei
Date of birth	17 June 1976
Place of birth	Kishinev (Republic of Moldova)
Citizenship	Republic of Moldova

Education

1983-1993	School #37 Kishinev, Republic of Moldova
03/06/1993	High-school graduation certificate #B 005260

Studies

1994-1999	Study of Physics Chair of Experimental Physics State University of Moldova Kishinev, Republic of Moldova
23/06/1999	Diploma degree certificate # AL 0021791
1999-2000	Master of Science Courses Institute of Applied Physics, Kishinev, Republic of Moldova
10/07/2000	Master of Science certificate #AM 0000323
2000-2006	PhD studies supervised by Prof. Dr. S. Horn Lehrstuhl für Experimentalphysik II, Universität Augsburg